A&A 652, A141 (2021)
https://doi.org/10.1051/0004-6361/202141543

Astronomy & Astrophysics

Refined physical parameters for Chariklo's body and rings from stellar occultations observed between 2013 and 2020⋆

B. E. Morgado[1,2,3], B. Sicardy[1], F. Braga-Ribas[4,3,2,1], J. Desmars[5,6,1], A. R. Gomes-Júnior[7,2], D. Bérard[1], R. Leiva[8,9,1], J. L. Ortiz[10], R. Vieira-Martins[3,2,11], G. Benedetti-Rossi[1,2,7], P. Santos-Sanz[10], J. I. B. Camargo[3,2], R. Duffard[10], F. L. Rommel[3,2,4], M. Assafin[11,2], R. C. Boufleur[2,3], F. Colas[6], M. Kretlow[12,10,13], W. Beisker[12,13], R. Sfair[7], C. Snodgrass[14], N. Morales[10], E. Fernández-Valenzuela[15], L. S. Amaral[16], A. Amarante[17], R. A. Artola[18], M. Backes[19,20], K.-L. Bath[12,13], S. Bouley[21], M. W. Buie[22], P. Cacella[23], C. A. Colazo[24], J. P. Colque[25], J.-L. Dauvergne[26], M. Dominik[27], M. Emilio[28,3], C. Erickson[29], R. Evans[19], J. Fabrega-Polleri[30], D. Garcia-Lambas[18], B. L. Giacchini[31,32], W. Hanna[33], D. Herald[12,33], G. Hesler[34], T. C. Hinse[35,36], C. Jacques[37], E. Jehin[38], U. G. Jørgensen[39], S. Kerr[33,40], V. Kouprianov[41,42], S. E. Levine[43,44], T. Linder[45], P. D. Maley[46,47], D. I. Machado[48,49], L. Maquet[6], A. Maury[50], R. Melia[18], E. Meza[1,51,52], B. Mondon[34], T. Moura[7], J. Newman[33], T. Payet[34], C. L. Pereira[4,3,2], J. Pollock[53], R. C. Poltronieri[54,16], F. Quispe-Huaynasi[3], D. Reichart[41], T. de Santana[1,7], E. M. Schneiter[18], M. V. Sieyra[55], J. Skottfelt[56], J. F. Soulier[57], M. Starck[58], P. Thierry[59], P. J. Torres[60,61], L. L. Trabuco[49], E. Unda-Sanzana[25], T. A. R. Yamashita[7], O. C. Winter[7], A. Zapata[62,63], and C. A. Zuluaga[44]

(Affiliations can be found after the references)

Received 14 June 2021 / Accepted 12 July 2021

ABSTRACT

Context. The Centaur (10199) Chariklo has the first ring system discovered around a small object. It was first observed using stellar occultation in 2013. Stellar occultations allow sizes and shapes to be determined with kilometre accuracy, and provide the characteristics of the occulting object and its vicinity.

Aims. Using stellar occultations observed between 2017 and 2020, our aim is to constrain the physical parameters of Chariklo and its rings. We also determine the structure of the rings, and obtain precise astrometrical positions of Chariklo.

Methods. We predicted and organised several observational campaigns of stellar occultations by Chariklo. Occultation light curves were measured from the datasets, from which ingress and egress times, and the ring widths and opacity values were obtained. These measurements, combined with results from previous works, allow us to obtain significant constraints on Chariklo's shape and ring structure.

Results. We characterise Chariklo's ring system (C1R and C2R), and obtain radii and pole orientations that are consistent with, but more accurate than, results from previous occultations. We confirm the detection of W-shaped structures within C1R and an evident variation in radial width. The observed width ranges between 4.8 and 9.1 km with a mean value of 6.5 km. One dual observation (visible and red) does not reveal any differences in the C1R opacity profiles, indicating a ring particle size larger than a few microns. The C1R ring eccentricity is found to be smaller than 0.022 (3σ), and its width variations may indicate an eccentricity higher than ∼0.005. We fit a tri-axial shape to Chariklo's detections over 11 occultations, and determine that Chariklo is consistent with an ellipsoid with semi-axes of $143.8^{+1.4}_{-1.5}$, $135.2^{+1.4}_{-2.8}$, and $99.1^{+5.4}_{-2.7}$ km. Ultimately, we provided seven astrometric positions at a milliarcsecond accuracy level, based on *Gaia* EDR3, and use it to improve Chariklo's ephemeris.

Key words. occultations – methods: observational – methods: data analysis – minor planets, asteroids: individual: Chariklo – planets and satellites: rings

1. Introduction

The Centaur (10199) Chariklo is a small object in our Solar System moving on an elliptical orbit between Saturn and Uranus, at heliocentric distances varying from 13.1 to 18.9 au. It was discovered in 1997 (Ticha et al. 1997), and is the largest Centaur known to date. From thermal infrared observations, its surface equivalent radius ranges between 109 and 151 km (Jewitt & Kalas 1998; Altenhoff et al. 2001; Campins & Fernández 2002; Sekiguchi et al. 2012; Bauer et al. 2013; Fornasier et al. 2013, 2014; Lellouch et al. 2017); the most recent solution of 121 ± 4 km (Lellouch et al. 2017) was obtained with the Atacama Large Millimeter/submillimeter Array (ALMA[1]).

From a stellar occultation observed in 2013, Braga-Ribas et al. (2014) reported the discovery of two dense and narrow rings (2013C1R and 2013C2R, hereafter C1R and C2R) surrounding Chariklo at 390 and 405 km from the body centre, respectively. This was the first time that rings had been observed elsewhere than around giant planets. Being narrow and dense, they bear some resemblance to some of Uranus' rings (Elliot et al. 1984; French et al. 1991). More on Chariklo's rings properties (orbital

⋆ Tables C.1, C.2 and lightcurves are only available at the CDS via anonymous ftp to cdsarc.u-strasbg.fr (130.79.128.5) or via http://cdsarc.u-strasbg.fr/viz-bin/cat/J/A+A/652/A141.

[1] https://www.almaobservatory.org/en/home/

radii and pole, width and opacity) is given by Bérard et al. (2017) and reviewed in Sicardy et al. (2018).

Another ring was discovered later around the dwarf planet (136108) Haumea (Ortiz et al. 2017), and there is evidence (yet to be confirmed) of a ring (or a dust shell) around the Centaur (2060) Chiron (Ortiz et al. 2015; Sickafoose et al. 2020). This raises new questions on the origins, dynamical evolution, and stability of these ring systems, which have been studied by several authors (see e.g. Pan & Wu 2016; Hyodo et al. 2016; Melita et al. 2017; Michikoshi & Kokubo 2017; Araujo et al. 2018; Sicardy et al. 2018, 2019 and references therein). Dynamical models are essential to address these questions and better understand the orbital evolution of ring particles around these small objects. On the other hand, new observations can be used to constrain these dynamical models and provide new insights into the origin and evolution of rings around small bodies.

Chariklo's ring system has a diameter of ~800 km, subtending about 80 milliarcseconds (mas) when projected in the sky plane as seen from Earth. As a consequence, resolved ground-based imaging of this system is extremely challenging with the currently available equipment. For instance, Sicardy et al. (2015) observed this system with SPHERE, an adaptive optics system mounted at the 8.2 m Very Large Telescope (VLT/ESO), and obtained point spread functions (PSFs) of 30–40 mas (corresponding to ~300–400 km at Chariklo's distance). These authors also observed the system with the *Hubble* Space Telescope (HST), with typical PSFs of 30 mas. None of these observations were able to detect Chariklo's rings or to find an extended system of cometary jets or tenuous dust around the body. In contrast, stellar occultations can achieve kilometre-scale resolutions and can provide stringent constraints on the size and shape of the main body and its astrometric position at the mas level. Moreover, optical depths and inner structures of the rings can be revealed.

Between 2013 and 2016, 13 stellar occultations by Chariklo's system were observed, of which only the occultation of 2013 June 03 (Braga-Ribas et al. 2014; Bérard et al. 2017) has more than two chord detections over C1R. As there was no occultation with three or more detections of the main body, Leiva et al. (2017) used five single-chord and double-chords occultations to derive possible 3D shapes of Chariklo's main body. Bérard et al. (2017) mentions that a two-chord occultation by CR1 was observed from Australia on 2016 October 01 (see Fig. 3 of that paper). This event was also a two-chord occultation on the main body, and was used by Leiva et al. (2017).

These authors derived four possible solutions for Chariklo's shape: (i) a sphere with radius $R = 129 \pm 3$ km; (ii) a Maclaurin spheroid with semi-axes $a = b = 143^{+3}_{-6}$ km and $c = 96^{+14}_{-4}$ km; (iii) a Jacobi ellipsoid with $a = 157 \pm 4$ km, $b = 139 \pm 4$ km, and $c = 86 \pm 1$ km; and (iv) a triaxial ellipsoid with $a = 148^{+6}_{-4}$ km, $b = 132^{+6}_{-5}$ km, and $c = 102^{+10}_{-8}$ km.

Bérard et al. (2017) confirmed the presence of Chariklo's rings and their geometry as published by Braga-Ribas et al. (2014). Moreover, for the first time they provided resolved opacity profiles of C1R, revealing a W-shaped structure, and found significant azimuthal width variations for that ring, with values ranging between 5.0 and 7.5 km. This is reminiscent of the ring width variations found among Uranus' dense rings, in particular its widest one, the ϵ ring (Nicholson et al. 2018).

In this paper we present the results of eight unpublished stellar occultations by Chariklo and its ring system observed between 2017 and 2020. It contains the analysis of three multi-chord detections of Chariklo's main body, two multi-chord detections of C1R, and one multi-chord detection of C2R. The parameters obtained here can be used to further constrain the dynamical models of the rings, and the size and shape of Chariklo.

In Sect. 2 we describe our prediction process and the observational campaigns. Section 3 details the reduction process. In Sect. 4 we present our results concerning Chariklo's rings, with the estimation of pole orientation (Sect. 4.1), C1R structures and global parameters (Sect. 4.2.1), and C2R global parameters (Sect. 4.3). Section 5 contains the analysis of Chariklo's 3D shape considering 11 stellar occultation chords obtained between 2013 and 2020. In Sect. 6 we present Chariklo's astrometric solution derived from our work. Our conclusions are provided in Sect. 7.

2. Predictions and observational campaigns

All the events presented here were predicted in the framework of the European Research Council (ERC) Lucky Star project[2], and are publicly available for the community. After 2016 the *Gaia* DR1 (GDR1) catalogue (Gaia Collaboration 2016b,a) was the source of the stellar positions for our prediction pipeline (Assafin et al. 2012; Camargo et al. 2014; Desmars et al. 2015). After December 2018, it was replaced by the *Gaia* DR2 (GDR2) catalogue (Gaia Collaboration 2018), and by *Gaia* EDR3 (GEDR3) after the beginning of 2021 (Gaia Collaboration 2021). Regular astrometric programmes were carried out at the European Southern Observatory (ESO), the Observatório do Pico dos Dias (OPD/LNA), and the Observatorio de Sierra Nevada (OSN), among others, to improve the ephemerides of various objects.

Selected events triggered observational campaigns, involving both fixed and portable telescopes that were deployed along the predicted shadow paths. In addition to professional astronomers, they also involved citizen astronomer communities, such as the International Occultation Timing Association (IOTA/Europe[3]), Planoccult[4], and Occult Watcher[5].

Chariklo's ephemeris was pinned down to the 5 mas level (~50 km at Chariklo's distance, Desmars et al. 2017) using previous stellar occultations published by Braga-Ribas et al. (2014), Leiva et al. (2017) and Bérard et al. (2017), GDR2, and the NIMA (Numerical Integration of the Motion of an Asteroid Desmars et al. 2015) integrator. This uncertainty, being smaller than the size of Chariklo, allowed the detection of multi-chord stellar occultations by Chariklo and its rings between 2017 and 2020.

Table 1 provides information related to the observed events. It lists the geocentric closest approach time (UTC), the *Gaia* EDR3 source identifier, and the geocentric International Celestial Reference System (ICRS) coordinates of the stars at occultation epoch, applying proper motion, parallax, and radial velocity (when available). The last column of the table lists the (*Gaia*) G magnitude of the stars, which can be compared to Chariklo's V magnitude, ~18.9.

Our campaigns involved sites in South and North America, Africa, and Oceania. The observations used a wide range of telescope sizes, from small portable telescopes (0.25–0.30 m) to large observatories facilities such as the Very Large Telescope (VLT, 8.20 m), Gemini North (8.10 m), Southern Astrophysical Research (SOAR, 4.10 m), Observatório Pico dos Dias (OPD,

[2] https://lesia.obspm.fr/lucky-star/index.php
[3] https://www.iota-es.de/
[4] https://lists.vvs.be/postorius/lists/planoccult.ls.vvs.be/
[5] https://www.occultwatcher.net/

Table 1. Occulted star parameters for each observed event, as obtained from *Gaia* EDR3.

Occ. date and time UTC	*Gaia* EDR3 source identifier	Right ascension [(1)]	Declination [(1)]	G mag
2020-06-19 15:51	6852214948874014720	$20^h\ 02^m\ 31^s.99612 \pm 0.21$ mas	$-22°\ 20'\ 41''.4784 \pm 0.14$ mas	15.569
2019-09-04 08:03	6766511277365829760	$19^h\ 27^m\ 42^s.15144 \pm 0.09$ mas	$-25°\ 29'\ 21''.2488 \pm 0.06$ mas	13.117
2019-08-08 21:41	6766365630734160896	$19^h\ 31^m\ 49^s.78464 \pm 0.11$ mas	$-25°\ 34'\ 26''.7724 \pm 0.09$ mas	15.158
2019-08-02 10:02	6766356933423996544	$19^h\ 33^m\ 07^s.47470 \pm 0.42$ mas	$-25°\ 34'\ 42''.3668 \pm 0.35$ mas	17.766
2017-08-24 02:59	6737213175138988672	$18^h\ 42^m\ 35^s.22729 \pm 0.18$ mas	$-31°\ 09'\ 50''.6837 \pm 0.14$ mas	17.468
2017-07-23 05:58	6737020112089260672	$18^h\ 48^m\ 09^s.22138 \pm 0.04$ mas	$-31°\ 26'\ 32''.4591 \pm 0.03$ mas	14.005
2017-06-22 21:18	6760223758801661440	$18^h\ 55^m\ 15^s.65251 \pm 0.04$ mas	$-31°\ 31'\ 21''.6706 \pm 0.03$ mas	14.223
2017-04-09 02:24	6757456459825426560	$19^h\ 04^m\ 03^s.62801 \pm 0.03$ mas	$-31°\ 17'\ 15''.2304 \pm 0.03$ mas	14.094

Notes. [(1)]The stars coordinates (RA and Dec) and their uncertainties were propagated to the occultation epoch with the formalism proposed by Butkevich & Lindegren (2014) using the parameters (e.g. proper motion, parallax, radial velocity) from *Gaia* EDR3 (Gaia Collaboration 2021).

1.60 m), and Danish/ESO (1.54 m). The observational circumstances (e.g. telescopes, instruments, stations, observers) are given in Appendix A.

3. Data analysis

We used classical photometric pipelines to extract the occultation light curves (Sect. 3.1). Abrupt opaque edges models, including the effects of diffraction, finite band width, exposure time, and stellar diameter, were fitted to the star dis- and reappearances behind Chariklo's main body. For ring occultations the apparent opacity is also an adjustable parameter. The timings obtained at the various stations define occultation chords, which are in turn used to constrain Chariklo's shape (Sect. 3.2) and the ring size and orientation is space (Sect. 3.3).

3.1. Calibration and aperture photometry

All the images were converted to the standard `fits` format. The video files (`ser` or `avi`) were converted using TANGRA v3.7.3 (Pavlov 2020) or Python codes based on ASTROPY v4.0.1 (Astropy Collaboration 2013). When available, calibration images (bias, dark, and flat-field) were used to correct the original images using standard Image Reduction and Analysis Facility (IRAF; Butcher & Stevens 1981) procedures.

The flux from the target stars was obtained by aperture photometry using the Platform for Reduction of Astronomical Images Automatically (PRAIA; Assafin et al. 2011) package. We note that during the occultation, the star and Chariklo images are blended together in the same aperture. The total flux from the star and Chariklo was normalised to unity outside the occultation, using a polynomial fit just before and after the event. Finally, nearby stars were used as photometric calibrators to correct for low-frequency sky transparency fluctuations. The resulting light curves are displayed in Appendix F.

3.2. Times and projection in the sky plane

The immersion ($t_{\rm imm}$) and emersion ($t_{\rm eme}$) times were determined using a Monte Carlo approach with uniformly distributed parameters to test a vast number of simulated models (~100 000) for which chi-squared statistics are computed. This was done with the Stellar Occultation Reduction Analysis (SORA) v0.1.2[6]

[6] Website: https://sora.readthedocs.io/

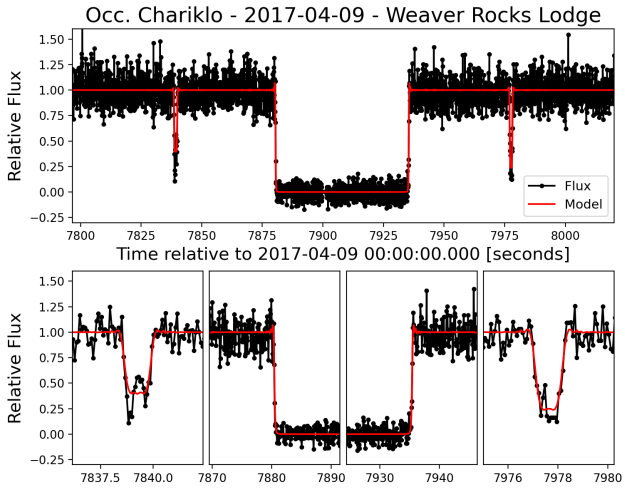

Fig. 1. Normalised light curve obtained at Weaver Rocks Lodge on 2017 April 09. The black dots show the observational data, while the red lines represent the fitted model. *Bottom panels*: zoom-in on 20 s centred on the immersion and emersion times and 2.5 s centred in each C1R detection. In this dataset there is no clear detection of C2R. All the light curves used in this work can be found in Appendix F.

package. The models consider a sharp-edge occultation model convolved with Fresnel diffraction, apparent stellar diameter (at Chariklo's distance), and finite integration time. For more details, see Braga-Ribas et al. (2013) and references therein.

To determine the ring parameters we also need to fit the apparent opacity (p') of the flux drop (Bérard et al. 2017). If insufficiently sampled, there is a large correlation between the apparent opacity of the rings and the duration of the detection ($\Delta t = t_{\rm eme} - t_{\rm imm}$). Thus, the positive ring detections have been divided into two groups: resolved detections with more than three points showing a significant drop in stellar flux during the occultation (higher than 3σ), and unresolved detections with fewer than three significant points. The three parameters ($t_{\rm imm}$, $t_{\rm eme}$, and p') can be fitted for the resolved detections, while the unresolved detections allow only the unambiguous determination of the central time ($t_{\rm mean} = \frac{1}{2}(t_{\rm eme} - t_{\rm imm})$). The obtained parameters for the main body and rings are listed in Table C.1, and an example of analysed light curve is provided in Fig. 1.

Using the Chariklo ephemeris (NIMA V.17), the GEDR3 star positions propagated to the event epoch, and the observer's position on Earth (latitude, longitude, and height), each occultation time is associated with a stellar position relative to Chariklo $(f,\ g)$, as projected in the sky plane. The position $(f,\ g)$ is expressed in kilometres, f (resp. g) being counted positively towards the local east (resp. north) celestial direction. We note that an offset in right ascension and declination, $(f_0,\ g_0)$, must be applied to the Chariklo ephemeris to account for errors on both the ephemeris and the star position (see discussion in Sect. 3.3). Thus, the final Chariklo-centric stellar position in the sky plane is given by $(f - f_0,\ g - g_0)$. Those positions are used in turn to determine the orbital parameters of Chariklo's rings and Chariklo's size and shape (see Sects. 4 and 5).

3.3. Projection in the ring plane

The ring parameters obtained in the sky plane (as derived from $t_{\rm imm}$, $t_{\rm eme}$, and p') are projected in the ring plane to derive the relevant parameters, more precisely: (i) the ring radial width, W_r; (ii) its distance r to Chariklo's centre; and (iii) its normal opacity, $p_{\rm N}$. The quantities W_r and r are calculated by projecting the corresponding $(f - f_0,\ g - g_0)$ in the ring plane, once the ring pole orientation $(\alpha_{\rm p},\ \delta_{\rm p})$ is known.

Finally, the ring opacity normal to its plane, $p_{\rm N}$, is given by

$$p_{\rm N} = p' \,.\, |\sin(B)|, \tag{1}$$

assuming a monolayer disc, where B is the ring opening angle ($B = 0°$ and $B = 90°$ corresponding to edge-on and pole-on viewings, respectively).

A relevant integral quantity, the equivalent width ($E_{\rm p} = W_r \,.\, p_{\rm N}$), can also be derived; it is related to the amount of material present in a radial cut of the ring. General discussions concerning these parameters are provided in Elliot et al. (1984) and French et al. (1991), and a more specific application to Chariklo's ring is presented in Bérard et al. (2017). The derived ring parameters are listed in Table C.2.

4. Ring structures and parameters

4.1. Ring pole

From the multi-chord ring detection of 2013 June 03, Braga-Ribas et al. (2014) derived two possible ring pole orientations, assuming the ring to be circular. In that case, the apparent ring oblateness ϵ' projected in the sky plane is given by

$$\epsilon' = 1 - \sin(B). \tag{2}$$

Long-term photometric trends (Duffard et al. 2014) allowed us to remove this ambiguity, providing $\alpha_{\rm p} = 10^{\rm h}\ 05^{\rm m} \pm 2^{\rm m}$ and $\delta_{\rm p} = +41°\ 29' \pm 13'$. This solution was later confirmed by stellar occultations observed between 2014 and 2016 (Bérard et al. 2017). We note that the ring pole orientation is in principle defined as being in the direction of the ring angular momentum, which in turn depends on the (unknown) direction of motion for the ring particles. This provides the possible solution $\alpha_{\rm p} + 180°$ and $-\delta_{\rm p}$. Here we arbitrarily choose the solution with $\delta_{\rm p} > 0$. This choice can be modified when the direction of motion is known, and does not influence our results.

The ring orbital parameters are obtained by fitting an ellipse to the occultation points, as seen in the sky plane. Five parameters are adjusted: the centre of the ellipse $(f_0,\ g_0)$; the apparent semi-major axis (a'); the apparent oblateness $(\epsilon' = 1 - b'/a')$; and the position angle (P) of the apparent semi-minor axis (b'), counted positively from the celestial north direction towards the celestial east.

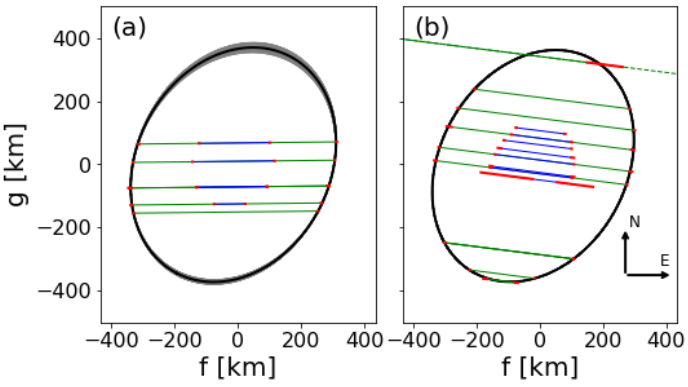

Fig. 2. Chords in the sky plane relative to Chariklo's main body (in blue), C1R (in green), and their uncertainties (in red). Ellipses were fitted to C1R points. The black line stands for the best-fit ellipse, and all the ellipses in the 1σ region are in grey. *Left panel*: event on 2017 June 22. *Right panel*: event on 2017 July 23. For the sake of clarity, some redundant chords on 2017 July 23 were not plotted.

In this work, and to avoid underdetermined fits, we only consider occultations that have at least six C1R detections, plus the discovery observation in 2013. These events were observed on 2017 June 22 and 2017 July 23, and are used to pin down the pole orientation and to assess possible ring eccentricities.

The fit uses a Monte Carlo approach with uniformly distributed parameters to test ~10 000 000 ellipses, thus providing χ^2 statistics, as well as the best fit corresponding to the minimum value, $\chi^2_{\rm min}$. The range $\chi^2_{\rm min}$ to $\chi^2_{\rm min} + 1$ then provides the marginal 1σ error bar for each parameter, which is the 68.3% confidence level for that parameter, ignoring the other four parameters, see Souami et al. (2020) and references therein for more details. For this project this step was done with the SORA V0.1.2 package.

Assuming that C1R is circular with radius $r_{\rm C1R}$ equal to the fitted a', we derive the pole orientation $(\alpha_{\rm p}, \delta_{\rm p})$ from B and P, using the equations

$$\sin(\delta_{\rm p}) = \cos(B)\cos(P)\cos(\delta) - \sin(B)\sin(\delta), \tag{3}$$

$$\cos(\alpha - \alpha_{\rm p}) = -[\sin(B) + \sin(\delta)\sin(\delta_{\rm p})]/[\cos(\delta)\cos(\delta_{\rm p})], \tag{4}$$

$$\sin(\alpha - \alpha_p) = -\cos(B)\sin(P)/\cos(\delta_{\rm p}), \tag{5}$$

where (α, δ) is Chariklo's ICRS position at epoch.

Figure 2 displays the best-fit ellipse on C1R for the events on 2017 June 22 and 2017 July 23. It also shows the sky plane projection of the obtained chords of the main body and rings. The obtained values are given in Table 2.

The results of Table 2 show a $\sim 1\sigma$ consistency with the discovery results of 2013 June 03. Moreover, the values from 2017 July 23 are more accurate than previously published by Braga-Ribas et al. (2014). The invariance of the derived pole orientation of C1R over time indicates that no significant eccentricity is detected for that ring. This is discussed more quantitatively later in Sect. 4.2.

4.2. C1 Ring structure

4.2.1. Radial profiles and eccentricity constraints

The high-resolution datasets presented here allow the study of the fine structure of C1R. The event of 2017 April 09, observed

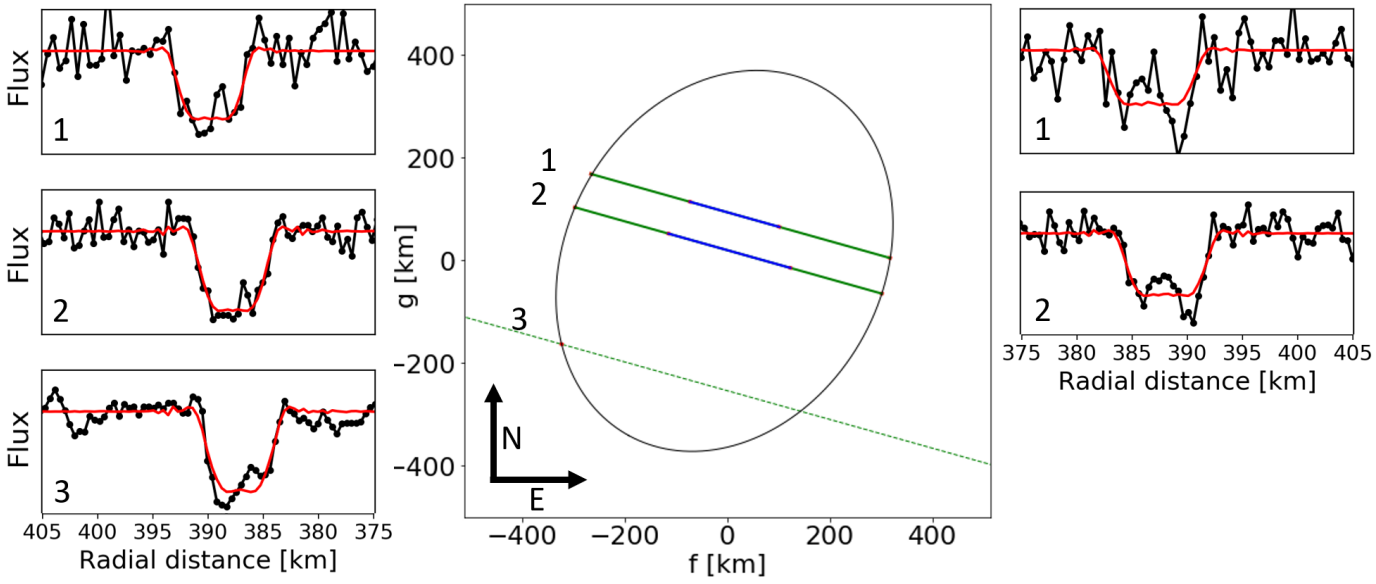

Fig. 3. Results of the 2017 April 09 event. The *central plot* displays the occultation chords projected in the sky plane for the main body (in blue), C1R (in green), and their uncertainties (in red). The black line is the best-fit ellipse to the C1R point, considering a fixed pole orientation (as determined in Sect. 4.1). *Side panels*: normalised radial ring profiles, projected in the ring plane, numbered as follows: Wabi Lodge (1), Weaver Rocks Lodge (2), and Hakos (3). *Right panels*: first detection (immersion) at each station. *Left panels*: second detections (emersion). As mentioned in Appendix A and shown in Appendix F, the Hakos light curve contains only the emersion detection of the ring due to bad weather conditions at immersion. The detections of W-shaped structures within the C1R are unambiguous.

Table 2. Ring pole orientation (ICRS) obtained from events with multi-chord detections of CR1 and their 1σ uncertainties.

Parameter	2013-06-03 [(a)]	2017-06-22	2017-07-23
$r_{\rm C1R}$ (km)	390.6 (03.3)	386.6 (12.3)	385.9 (00.4)
P (°)	−61.54 (0.10)	−62.13 (3.46)	−60.85 (0.11)
B (°)	+33.77 (0.41)	+52.33 (1.97)	+49.91 (0.11)
α_p (°)	151.25 (0.50)	149.46 (2.60)	151.03 (0.14)
δ_p (°)	+41.48 (0.22)	+40.98 (2.12)	+41.81 (0.07)
n.° det.	14	12	23[(b)]
$\chi^2_{\rm pdf}$	1.48	1.88	2.55

Notes. Where $r_{\rm C1R}$, P, and B stand for the C1R radius, the position angle of the pole, and the ring opening angle, respectively. [(a)]Values from Braga-Ribas et al. (2014). [(b)]The grazing chords were not used in the fit.

from Namibia, highlights the detection of such structures. During this event we had five detections of C1R; as this is unsuitable for fitting all the ellipse parameters, we fixed the pole orientation as obtained at 2017 July 23 to determine the centre position (f_0, g_0). With the fitted centre it was possible to project the chords in the sky plane to the ring plane.

The untypical low velocity of the 2017 April 09 occultation (~5 km s^{-1}) allowed us to probe Chariklo's ring with a resolution (Δr) of ~0.5 km per data point for the observations made at Wabi Lodge, Weaver Rocks Lodge, and Hakos. In this event, clear W-shaped structures appear in the different observations (see Fig. 3 for more details).

From the occultation of 2017 July 23, the datasets from Danish telescope (visual and red filters) and from OPD provided a clear detection of similar W-shaped structures within C1R (see Fig. 4 for details). The occultation's radial velocity at these stations allowed us to probe Chariklo's ring with a resolution (Δr) of ~1.0 km in the ring plane per data point. The VLT telescope had Δr on C1R of 2.2 km (exposure time of 0.1 s), so no clear structures were detected.

Using the resolved C1R profiles, we derive a mean radial width of ~6.9 km, with extreme values varying between ~4.8 and ~9.1 km for C1R, see Fig. 5.

For order of magnitude estimation, we assume that part of the width variation is associated with a $m = 1$ mode, in which case $W_r \sim [1 - q_e \cos(f)]\delta a$, with $q_e = e + a\partial e/\partial a$, where δe and δa are the variations in eccentricity (e) and semi-major axis (a) across the ring. By analogy with the eccentric ringlets of both Uranus and Saturn, we can assume that $a\partial e/\partial a \gg e$ (French et al. 1986). Adopting $\Delta W_r = 3.9$ km and $a = r_{\rm C1R} = 385.6$ km, we obtain $\delta e \sim \delta W_r/2a \approx 0.005$. Relying again on Uranus and Saturn as analogues, we expect e to be a few times δe (i.e. of the order of 0.01–0.02). This corresponds to full radial excursions of ~10 km for the C1R ring. This is an easily detectable quantity, but with the difficulty that Chariklo's centre of mass must be pinned down at better than that distance. These numbers are model dependent and should be taken with caution.

4.2.2. Two-band resolved profiles of C1R

The 2017 July 23 event was observed at the 1.54-meter Danish telescope at La Silla, using a dual system with a visible band (0.45–0.65 μm) and a red band (0.70–1.00 μm), see Skottfelt et al. (2015). Figure 6 displays the C1R and C2R radial profiles at immersion and emersion in both bands.

A visual inspection of Fig. 6 clearly reveals the W-shaped structure of the C1R radial profiles. No significant differences between the two bands appear, as confirmed by the fitted parameters of the rings (see Tables C.1 and C.2), where no significant differences are noted at the 1σ level.

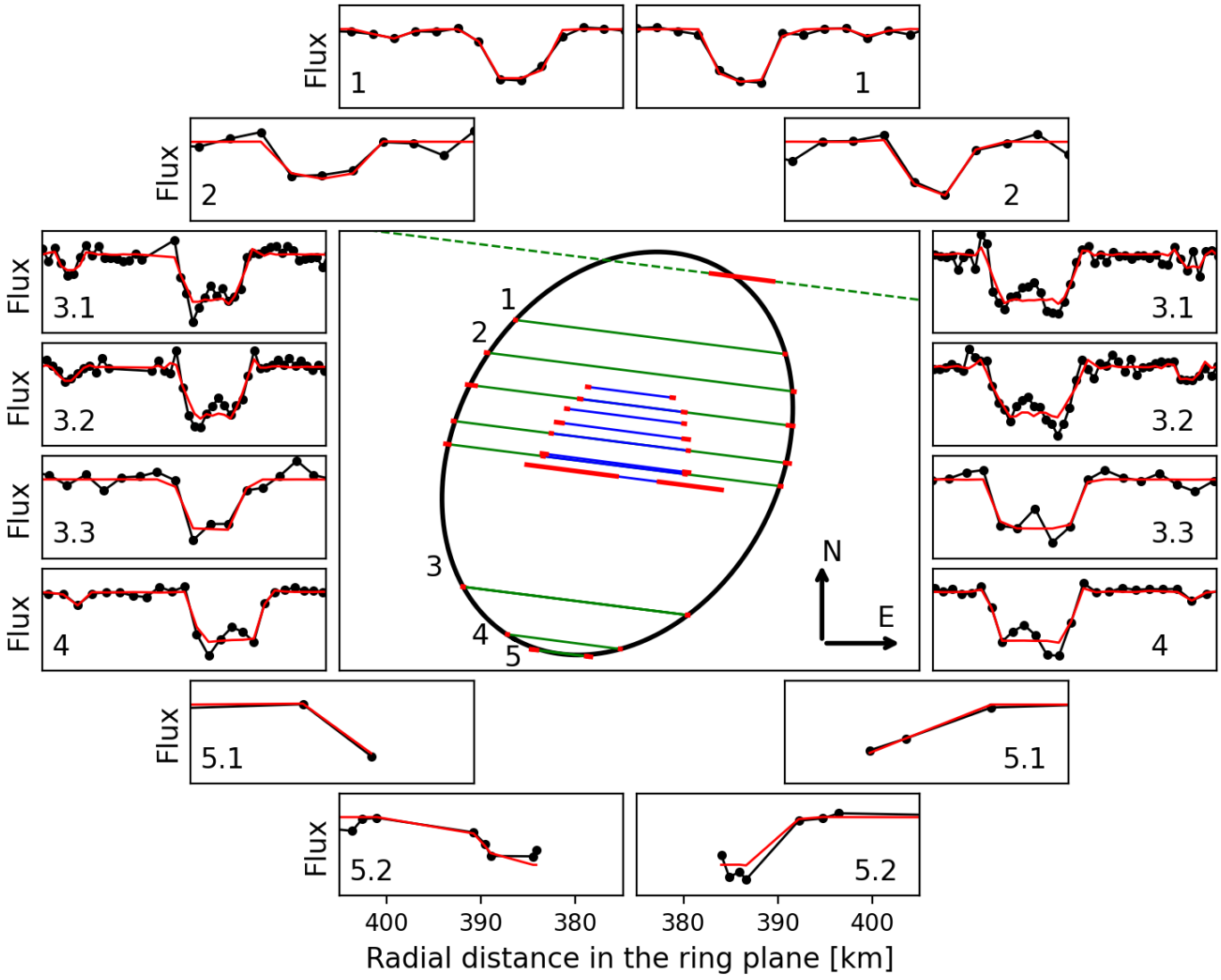

Fig. 4. Same as Fig. 3 for the 2017 July 23 event. The side panels are numbered as follows: Cerro Paranal (1), Tolar Grande (2), La Silla (3), Observatório Pico dos Dias (4), and Cerro Tololo (5). The observations on La Silla were made using the Danish telescope dual experiment in the visual (3.1) and red bands (3.2), and using a 1 m telescope (3.3). *Left panels*: first detection (immersion) at each station. *Right panels*: second detections (emersion). The observations on Cerro Tololo grazed over C1R, and were made using the SARA (5.1) and PROMPT (5.2). For the sake of clarity, some redundant chords were visually suppressed.

The similarity of the radial profiles of C1R in the two bands indicates that this ring contains mostly particles larger than a few microns (Elliot et al. 1984). This is expected by analogy with the dense and narrow Saturnian or Uranian rings. The local Keplerian shear of the velocity field inside Chariklo's rings is similar to that encountered in Saturn's or Uranus' rings (Sicardy et al. 2018). Moreover, water ice seems to be a major component of Chariklo's main ring (Duffard et al. 2014), as is the case for Saturn's (and probably Uranus') rings. Thus, comparable collisional processes to those found in Saturn's or Uranus' rings are expected in C1R, and consequently comparable particle size distributions. In particular, the opacities of the dense rings of Saturn and Uranus are dominated by centimetre- to metre-sized particles, with a very small amount of dust for the rings of both Saturn (Cuzzi et al. 2018) and Uranus (Esposito et al. 1991), which are in line with our finding for C1R.

4.3. C2 Ring structure

Chariklo's C2R is narrower than C1R, with an orbital radius that was previously estimated to 405 km and an equivalent width that can vary between 0.1 and 1 km (Braga-Ribas et al. 2014; Bérard et al. 2017). This small size makes it very difficult to detect this ring. In this work we present unresolved detections, but most of the previous observations did not detect it. We obtained here the first multi-chord detection of C2R during the 2017 July 23 occultation.

As there is no resolved detection of C2R in this work, only the mid-times of each detection could be obtained. The ring radial width and opacity have large uncertainties and are highly correlated. A better-defined quantity is then the equivalent width, for which we obtain a mean value 0.117 ± 0.08 km from the values listed in Table C.2, all obtained during the 2017 July 23 event.

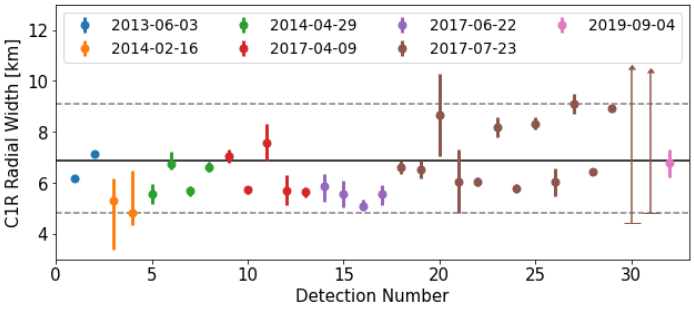

Fig. 5. C1R radial width for all the obtained resolved detections. The PROMPT and SARA values only provide lower limits to the radial width. The black line represents the mean value of W_r (6.9 km); the grey dashed lines give the minimum and maximum values (4.8 and 9.1 km).

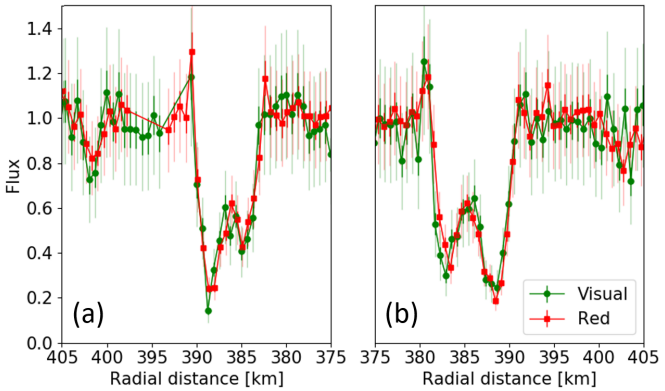

Fig. 6. Normalised radial profiles of C1R and C2R projected in the ring plane, as observed from the 1.54 m Danish telescope during the 2017 July 23 event. The green points are for the visual channel (0.45–0.65 μm), the red points for the red channel (0.70–1.0 μm). The darker (resp. lighter) error bars are for the 1σ (resp. 3σ) level stemming from the S/N of the target source and the calibrators. *Panels a and b*: first detection (immersion) and second detection (emersion), respectively. There is agreement between the visual and the red channels in both detections.

Using the same approach described in Sects. 4.1 and 4.2.1, we fitted the best ellipse to obtain the global orbital parameters of C2R, and compared the resulting centre, position angle, and pole with those obtained for C1R during the same event. Figure 7 (panel a) displays the C2R chords and the corresponding best-fit ellipse. A close-in view showing the fitted centres of C1R and C2R in the sky plane (panel b) reveals an offset of 2.28 km between those two centres at the $\sim 3\sigma$ level. The radial offset Δr between C2R and C1R in the ring plane versus the longitude, deduced from the respective elliptical fits, is displayed in panel c. The grey area contains the 1σ uncertainty region for Δr, considering the respective uncertainties on the C1R and C2R fits.

Table 3 provides the fitted parameters obtained independently for C1R and C2R. We find that the two ring pole orientations are mutually consistent at a 1σ level. The 2.28 km offset between the rings centres might be indicative of a differential eccentricity of the order of $2.28/386 \sim 0.006$ between the two rings. However, we estimate that this 3σ level detection remains marginally significant. Finally, we find an average radial distance ΔR between C1R and C2R of 14 km, with a 1σ uncertainty interval of ~10–19 km, which is in agreement with the mean value of 14.8 km found by Bérard et al. (2017).

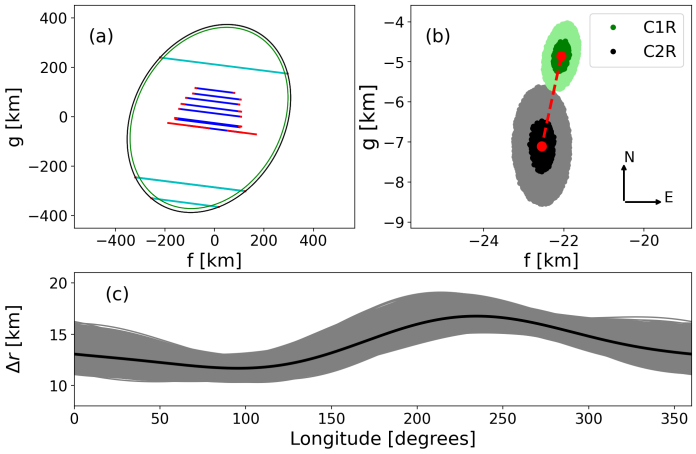

Fig. 7. Comparison between C1R and C2R. *Panel a*: occultation chords of the 2017 July 23 event detected, for Chariklo's main body (blue) and for the C2R ring (cyan). The uncertainties at the extremities of the chords are indicated in red. For sake of clarity, the C1R chords are not reproduced here, and can be seen in Figs. 2 and 4. The fitted ellipses to the C2R is drawn in black. The 1σ uncertainty region of that fit is indistinguishable from the black line thickness at this scale. The best-fit ellipse to the C1R ring detections is shown in green. *Panel b*: fitted centres of C1R (green) and C2R (black) in the sky plane. The darker colours stand for the simultaneous 1σ uncertainty regions (corresponding to the $\chi^2_{\rm min}$ + 2.3 criterion), while the lighter colours stand for the 3σ regions ($\chi^2_{\rm min}$ + 11.4 criterion). The red dashed line shows a 2.28 km offset between the C1R and C2R centres. *Panel c*: radial difference Δr (in the ring plane) between C2R and C1R vs. the longitude, deduced from the elliptical fits of panel a. The grey zone delimits the 1σ region associated with the uncertainties on C1R and C2R. It shows that no significant radial distance variations between C1R and C2R are detected at that level.

Table 3. Parameters obtained on 2017 July 23 from fitting ellipses over C1R and C2R projections in the sky plane.

Parameter	C1R	C2R
f_0 (km)	−22.0 (0.1)	−22.5 (0.2)
g_0 (km)	−04.8 (0.1)	−07.1 (0.4)
r (km)	385.9 (0.4)	399.8 (0.6)
P (°)	−60.85 (0.11)	−61.18 (0.19)
B (°)	+49.91 (0.11)	+49.99 (0.16)
$\alpha_{\rm p}$ (°)	151.03 (0.14)	150.91 (0.22)
$\delta_{\rm p}$ (°)	+41.81 (0.07)	+41.60 (0.12)
n.° det.	23	08
$\chi^2_{\rm pdf}$	2.55	0.68

Considering the multi-band detection of C2R with the Danish telescope, similar to the findings for C1R, no significant differences between the two filters appear, but due to its poorer detection level, differences can be hidden within the noise.

4.4. Search for faint ring material between C1R and C2R

Our best light curves in terms of time resolution and S/N were obtained during the 2017 July 23 event at the VLT, OPD, and Danish telescope (La Silla). They can be used to detect or place an upper limit of material orbiting in the gap between C1R and C2R. We assume that this putative semi-transparent material is concentric and co-planar to C1R and C2R.

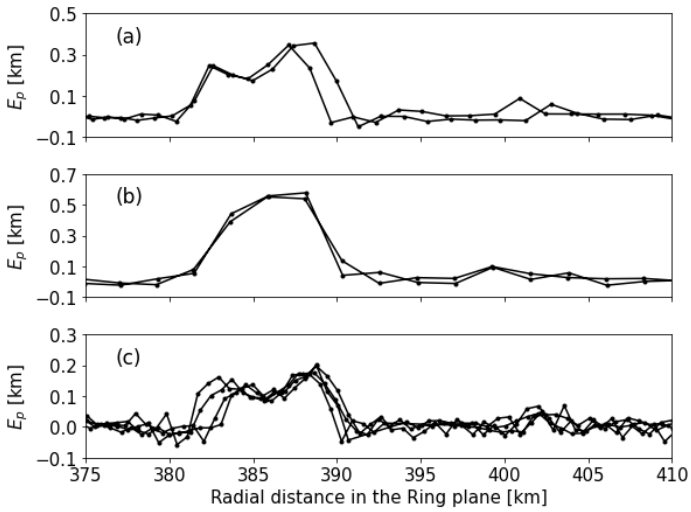

Fig. 8. Equivalent width of ring material over the radial distance in the ring plane for the observations in OPD/LNA (*a*), VLT/ESO (*b*) and Danish/ESO (*c*). We determine a 3σ upper limit of semi-transparent uninterrupted material between C1R and C2R with normal opacity of 0.006.

Following similar procedures to those described in Bérard et al. (2017), we convert each data-point (i) from flux to equivalent width (E_p) using Eq. (6), where $\phi(i)$ is the normalised light-flux, and $\Delta r(i)$ is the radial resolution in the ring plane travelled by the star during one exposure ($\Delta t(i)$),

$$E_{\rm p}(i) \;=\; \frac{|\sin(B)|}{2} \,.\, [1-\phi(i)] \,.\, \Delta r(i) \,. \tag{6}$$

The top panel a of Fig. 8 contains a plot of $E_{\rm p}(i)$ over the radial distance in the ring plane $R(i)$ for the observation at OPD. The 1σ limit for the equivalent width ($E_p(1\sigma)$) for the region between C1R and C2R in the ring plane (between 391 and 399 km) was 24 m; this means that if there were an uninterrupted ring between C1R and C2R with normal opacity greater than ($p_{\rm n}$) of 0.003 (0.009) it would have been detected with a 1σ (3σ) confidence level. As for the VLT observation with a Δr of 2.2 km, it only contains three data points between C1R and C2R for each detection. For this dataset a ring with normal opacity of 0.011 would have been detected within 3σ confidence level, as can be seen in the middle panel b in Fig. 8.

Another approach is the combination of some data to increase the quality of the measurement. As shown in Sect. 4.2.2, the Danish observations in two different filters are virtually the same (within the errors), meaning that these two observations can be combined to improve the quality of the data. Using the combination of the two light curves illustrated in the bottom panel c in Fig. 8 we obtain an $E_{\rm p}(1\sigma)$ of 16 m. Ring material between C1R and C2R with normal opacity greater than 0.002 (0.006) would have been detected at 1σ (3σ) confidence level.

5. Chariklo's size, shape, and rotational parameters

Between 2013 and 2020 Chariklo was the target of several successful stellar occultations. This allowed us to go further than only the determination of its apparent size and shape. It let us determine Chariklo's 3D shape. We were also able to analyse the centre position of Chariklo and how it compares with its rings' centre, thus giving us constraints on Chariklo rings' excentricity. Finally, we evaluated Chariklo's rotational parameters (rotational light curve amplitude) to see how our model compares with previous observations.

5.1. Chariklo's 3D shape

First, we consider that Chariklo's pole orientation is the same as its rings and, as we show in Sect. 4.1, the C1R pole orientation can be considered fixed between 2013 and 2017.

As an initial guess, we consider that the centre of Chariklo and its rings are the same. This assumption allows us to consider 11 stellar occultations that had at least one chord over Chariklo's main body and at least two ring detections. The only exception was the occultation on 2019 August 08 that had five detections of the main body, but no ring detection. In Sect. 5.3 we analyse Chariklo's centre further, and use it to derive an upper limit to Chariklo's rings eccentricities.

We also consider that Chariklo's rotational period is known, and equals 7.004 ± 0.036 (Fornasier et al. 2014). Even though we know Chariklo's period, the period uncertainty is large enough that its rotational phase cannot be determined at the moment of each occultation. In other words, it can be any value between 0 and 360 degrees.

Our analysis considers the rotational elements as described in Archinal et al. (2018). The angle $W(t)$ specifies the position of the prime meridian (in this work chosen to be in the direction of the longest axis) on a given date (considering light time between Chariklo and the observer), W_0 is the value of W at the reference epoch ($t_{\rm ref}$), and $\dot{W}$ stands for the rotation rate, here expressed in degrees per days:

$$W(t) = W_0 + \dot{W}(t - t_{\rm ref}) \,. \tag{7}$$

The reference epoch was chosen as the time of the first stellar occultation considered here, 2013 June 03 06:25:00 UTC (2456446.767361111 JD), to minimise error propagation. We consider a given 3D ellipsoidal model with semi-axis $a > b > c$, rotating around its smallest axis (c). We project this ellipsoid in the sky plane and determine its projected limb as the points where the gradient of the normal to the direction to the observer is equal to zero.

The model limb is then compared with the occultations chords, and chi-squared statistics are computed using

$$\chi^2 = \sum_i^N \frac{(r_i - r'_i)^2}{\sigma_i^2 + \sigma_{\rm model}^2}, \tag{8}$$

where r_i is the radial distance of the ith observed chord extremity, r'_i is the radial distance of the ellipsoid limb, σ_i is the observed radial uncertainty at each extremity point, and $\sigma_{\rm model}$ consists of the uncertainty of our ellipsoidal model in contrast with Chariklo's real 3D shape, for instance the existence of topographic features within Chariklo's surface. The value of $\sigma_{\rm model}$ was estimated iteratively as 3 km, so the resulting χ^2 per degree of freedom would be close to 1.

We compute this for 10 000 000 models, varying a, b, c, W_0, and $\dot{W}$. As we do not intend to fit the rotation rate, we let it vary between 1227.20 and 1239.95 deg days^{-1}. This value was obtained considering a period between 6.968 and 7.040 h, as provided by Fornasier et al. (2014). For the other parameters, we let a, b, and c vary in the range of 125 ± 50 km and W_0 between 0 and 360 degrees.

Our best-fitting value was the ellipsoid with semi-axis equals to $143.8^{+1.4}_{-1.5}$, $135.2^{+1.4}_{-2.8}$, and $99.1^{+5.4}_{-2.7}$ km with $\chi^2_{\rm pdf}$ equal to 0.688. Figure 9 shows this ellipsoid fitted to the observational data. The

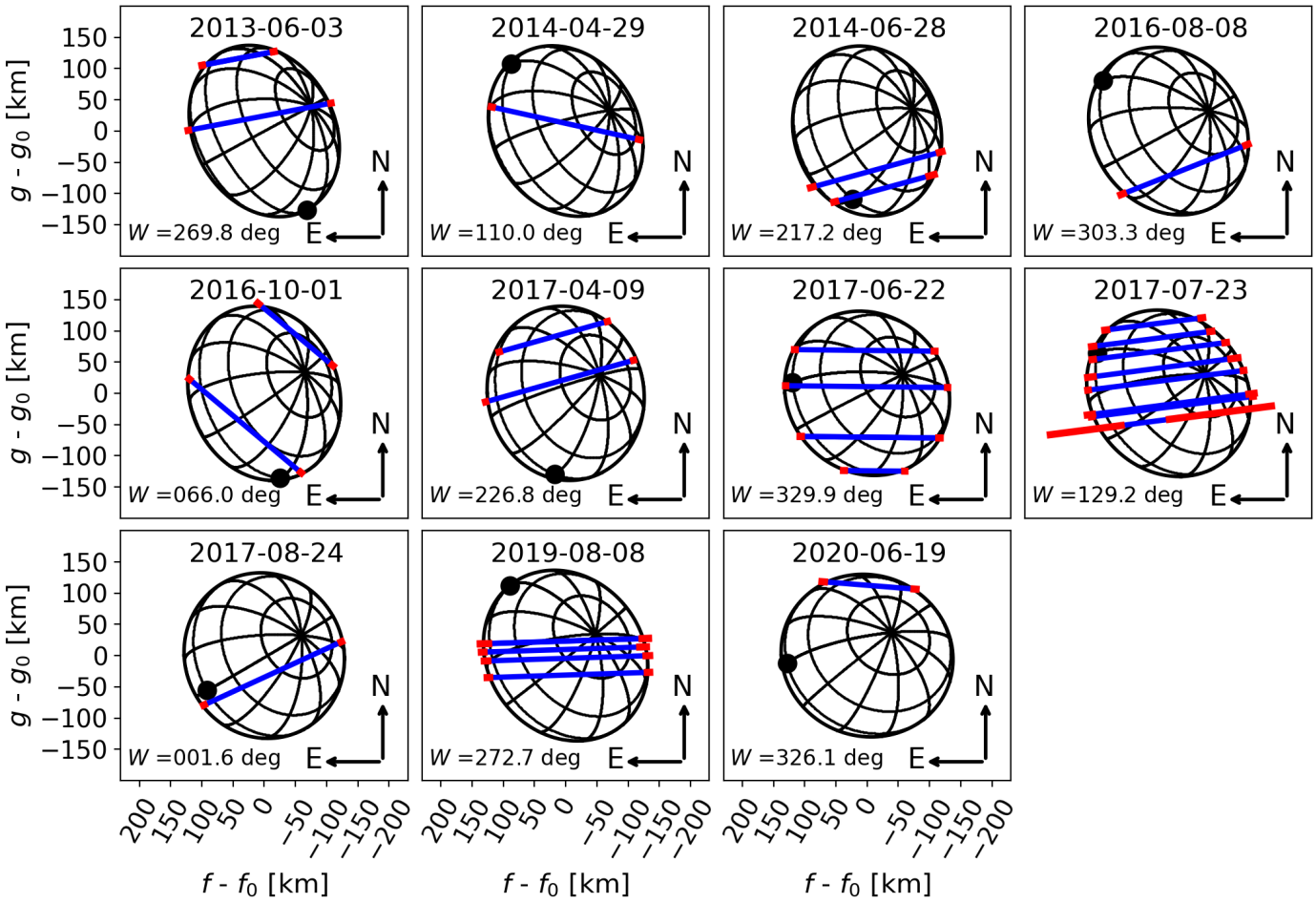

Fig. 9. Ellipsoidal model that best fits the 11 stellar occultations observed between 2013 June 23 and 2020 June 19. Each panel corresponds to an occultation event identified by the time stamp. The blue lines stand for the observed chords with their uncertainties in red. The black dot indicates the intersection between the equator and the prime meridian, which is used as the reference to define the rotation angle W, indicated at the lower left.

standard deviation of the radial residuals was 4.11 km (2.8% considering a volume equivalent radius of 124.8 km), with a maximum value of 7.78 km and a minimum of −5.52 km, this can indicate topographic features of this range on Chariklo's surface.

5.2. Chariklo's density

After fitting an ellipsoid to Chariklo, the first thing that becomes clear is that Chariklo does not have a shape corresponding with the equilibrium figure of a Maclaurin spheroid (where a would be equal to b). Instead, if we consider the Jacobi figure, the expected uniform density (ρ) of Chariklo would be $1.55^{+0.05}_{-0.08}$ g cm^{-3}, as can be calculated with Eq. (9),

$$\Omega = \frac{2\pi}{G\rho T^2} = \beta\gamma \int_0^\infty \frac{u}{(1+u)(\beta^2+u)\Delta(u,\beta,\gamma)} \mathrm{d}u \,, \quad (9)$$

$$\Delta(u,\beta,\gamma) = \sqrt{(1+u)(\beta^2+u)(\gamma^2+u)} \,, \quad (10)$$

where G is the gravitational constant, T is the rotational period, β and γ respectively stand for the semi-axis ratios b/a and c/a (more details in Sicardy et al. 2011; Ortiz et al. 2017 and references therein). This density is not consistent with the expected value, between 0.79 and 1.04 g cm^{-3}, of a body with a rotational period (T) of 7.004 h. For a stable Jacobi ellipsoid the shapes should lie with the dimensionless parameter Ω between 0.284 and 0.374 (Tancredi & Favre 2008), instead of 0.191 as obtained in our analysis.

On the other hand, one possibility is that the Chariklo ring particles would be close to the 1/3 resonance with the central body Sicardy et al. (2019). This means that the particles complete one revolution, while the body completes three rotations. In this context, an ellipsoid with a semi-axis of 143.8, 135.2, and 99.1 km should have a density between 0.73 and 0.85 g cm^{-3}, so the 1/3 resonance would be between 385 and 405 km, the region where the Chariklo ring particles are. These are indications that the hydrostatic equilibrium of a homogeneous body does not dominate Chariklo's shape.

5.3. Comparing Chariklo's centre with its rings' centre

As mentioned in Sect. 5.1, we considered that Chariklo's centre is the same as its rings' centre. Any deviation from this would appear as a systematic effect unique to each stellar occultation. In extreme cases (tens of kilometres), this would also preclude a unique solution with the methodology applied. This is not the case, as can be seen from Fig. 9.

We used our derived 3D model and fitted it for the centre on the chords of the 2017 July 23 multi-chord detection to check for small systematic effects. Here we compare the fitted value for

Table 4. Rotational light curve amplitudes from the literature.

Date	Δmag	Reference	Alias
1997–05	<0.02	Davies et al. (1998)	D98
1999–03	<0.05	Peixinho et al. (2001)	P01
2006–06	0.13 ± 0.03	Galiazzo et al. (2016)	G16
2013–06	0.11 ± 0.02	Fornasier et al. (2014)	F14
2015–07	0.06 ± 0.02	Leiva et al. (2017)	L17

Notes. The alias column is a simplified reference name, the first letter of the main author's name, plus the two last digits of publication year.

Chariklo main body and the centre obtained for its rings (values in Table 3). We obtain a radial difference between the main body and C1R of $2.46^{+2.86}_{-2.07}$ km in the sky plane considering a 1σ confidence level. At a 3σ level, this value is between zero and 8.41 km. If we consider that this offset is in the ring plane, this could be translated to a $2.51^{+2.84}_{-2.50}$ km difference, in a 3σ confidence level ranging between 0 and 8.55 km.

The 1σ (3σ) region's limit can give us hints about the maximum difference between Chariklo's centre and the centre of its rings. This value cannot be larger than 5.35 (8.55) km at the moment of the detected occultations. These values give us an upper limit of the eccentricity of C1R rings of about 0.014 (0.022).

Applying the same analysis to C2R as observed on 2017 July 23, we obtain a maximum radial distance of 3.27 (6.84) km in the ring plane. This represents an upper limit of about 0.0082 (0.0171) for C2R eccentricity considering a 1σ (3σ) confidence level.

5.4. Rotational light curve amplitude

Considering Chariklo's rotational light curve, we can check if our ellipsoidal model can explain the light curve amplitude provided by Leiva et al. (2017) as observed by Davies et al. (1998), Peixinho et al. (2001), Galiazzo et al. (2016), Fornasier et al. (2014) and Leiva et al. (2017), and listed in Table 4.

We calculate the magnitude amplitude using Eq. (11) as derived by Fernández-Valenzuela et al. (2017) and references therein,

$$\Delta m = -2.5 \log \frac{A_{\rm min} p_{\rm V} + A_{\rm r}(I/F)}{A_{\rm max} p_{\rm V} + A_{\rm r}(I/F)}, \quad (11)$$

where $A_{\rm min}$ and $A_{\rm max}$ respectively stand for the smallest and largest area covered by the 3D model, and $A_{\rm r}$ is the area covered by Chariklo's rings. Here we assume Chariklo's geometric albedo ($p_{\rm V}$) to be 3.7% and the ring reflectivity (I/F) to be 4.9% (Leiva et al. 2017). As shown in Fig. 10 our 3D model can explain the observed light curve amplitude. Any slight difference can be associated with albedo variegation.

6. Astrometric positions

A valuable by-product of stellar occultations is the mas-level precision of the occulting body astrometry, especially since the *Gaia* DR2 and EDR3 catalogues provide the stars' positions to sub-mas-level precision (Desmars et al. 2019; Herald et al. 2020; Rommel et al. 2020). This means a significant improvement of the occulting body ephemerides, which in turn allows better predictions for future events in a virtuous loop.

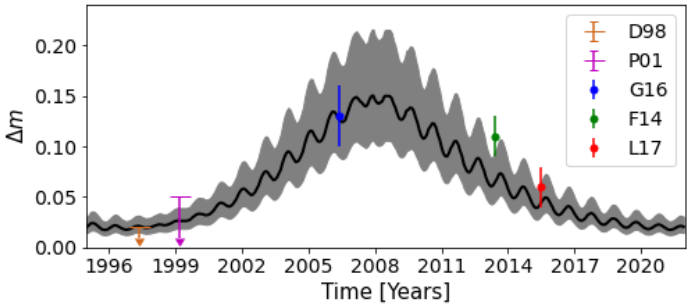

Fig. 10. Rotational light curve amplitude variations over the years. In black is our best-fit ellipsoidal model, and in grey all the ellipsoids within the 1σ region. We compare our model with the observation detailed in Table 4.

We obtained Chariklo's astrometric positions from seven stellar occultations observed between 2017 and 2020, assuming that the centre of Chariklo coincides with the centre of C1R. We note that the 2019 September 04 occultation only gives the egress detection of C1R, so that no astrometric constraints can be derived from that event (see details in Appendix E). Table 5 lists the positions obtained and their associated uncertainties. These uncertainties stem from the uncertainties on the fitted ring centre (σf_0, σg_0) and the statistical uncertainties on the star positions propagated to the occultation epoch (see Table 1). We note that the resulting uncertainties are usually at the sub-mas level, corresponding to a few kilometres at Chariklo's distance, where 1 mas ~10 km.

These positions were used to improve Chariklo's ephemeris using the NIMA software (Desmars et al. 2015). The corresponding bsp file (NIMA v.19) can be downloaded from the Lucky Star website[7]. The updated ephemeris provides a propagated uncertainty on Chariklo's position of 2 mas in right ascension and declination, as of January 2022. This corresponds to roughly 20 km at Chariklo's distance.

7. Conclusions

This paper presents results from eight unpublished stellar occultations by Chariklo and its rings, observed between 2017 and 2020. Our main results are as follows:

(i) For the first time, we detected stellar occultations with three (or more) chords over Chariklo's main body.
(ii) We obtained the second and third multi-chord detections of C1R since the discovery of Chariklo's rings (2013 June 03).
(iii) We obtained multi-chord detections of C2R for the first time.
(iv) We obtained the first simultaneous multi-band observation of Chariklo's rings.
(v) New astrometric data for the Chariklo system was obtained from all the detected stellar occultations, including two single-chord and one double-chord events.

Table 6 contains a summary of our main results. We determined a Chariklo's rings pole orientation consistent with, and more precise than those previously determined by Braga-Ribas et al. (2014). We could not refute that Chariklo's ring are circular within our measurement errors. We estimate an upper 3σ limit of 0.022 for the eccentricity of C1R. By analogy with Uranus' and Saturn's ringlets, and from its width variations we estimate an eccentricity greater than ~0.005 for that ring which remains, however, model dependent.

[7] https://lesia.obspm.fr/lucky-star/obj.php?p=624

Table 5. Astrometric Chariklo's positions for each event.

Date and time UTC	Right ascension [(a)]	Declination [(a)]
2020-06-19 15:51:00.000	$20^h\ 02^m\ 32^s.0002322 \pm 0.339$ mas	$-22°\ 20'\ 41''.488487 \pm 0.227$ mas
2019-08-08 21:41:00.000	$19^h\ 31^m\ 49^s.7910264 \pm 0.227$ mas	$-25°\ 34'\ 26''.785014 \pm 0.544$ mas
2019-08-02 10:02:00.000	$19^h\ 33^m\ 07^s.4812764 \pm 0.872$ mas	$-25°\ 34'\ 42''.519146 \pm 1.187$ mas
2017-08-24 02:59:00.000	$18^h\ 42^m\ 35^s.2371826 \pm 0.426$ mas	$-31°\ 09'\ 50''.561462 \pm 0.432$ mas
2017-07-23 05:58:00.000	$18^h\ 48^m\ 09^s.2288885 \pm 0.103$ mas	$-31°\ 26'\ 32''.437598 \pm 0.096$ mas
2017-06-22 21:18:00.000	$18^h\ 55^m\ 15^s.6602082 \pm 0.116$ mas	$-31°\ 31'\ 21''.621802 \pm 0.110$ mas
2017-04-09 02:24:00.000	$19^h\ 04^m\ 03^s.6255610 \pm 0.129$ mas	$-31°\ 17'\ 15''.257638 \pm 0.127$ mas

Notes. [(a)]The positions assume the EDR3 star positions given in Table 1.

Table 6. Summary of the obtained parameters for Chariklo and its rings.

	Parameter	Value	Comments
C1 Ring	Radius	385.9 ± 0.4 km	See Sect. 4.1
	Pole orientation (RA)	151.03 ± 0.14 deg	See Sect. 4.1
	Pole orientation (Dec)	+41.81 ± 0.07 deg	See Sect. 4.1
	Mean width	6.86 km	See Sect. 4.2.1
	Width variation	$4.8 \leq W_r \leq 9.1$ km	See Sect. 4.2.1
	Eccentricity	$0.005 \leq e_{\rm C1R} \leq 0.022$	See Sects. 4.2.1 and 5.3
	Particle's size	>1.0 micron	See Sect. 4.2.2
Gap between C1R and C2R	Radial distance between rings	$13.9^{+5.2}_{-3.4}$ km	See Sect. 4.3
	Equivalent width of material in gap	<0.048 km	See Sect. 4.4
C2 Ring	Radius	399.8 ± 0.6 km	See Sect. 4.3
	Pole orientation (RA)	150.91 ± 0.22 deg	See Sect. 4.3
	Pole orientation (Dec)	+41.60 ± 0.12 deg	See Sect. 4.3
	Equivalent width	0.117 ± 0.080 km	See Sect. 4.3
	Eccentricity	<0.017	See Sect. 5.3
Chariklo	a (Semi-major axis)	$143.8^{+1.4}_{-1.5}$ km	See Sect. 5.1
	b (Semi-median axis)	$135.2^{+1.4}_{-2.8}$ km	See Sect. 5.1
	c (Semi-minor axis)	$99.1^{+5.4}_{-2.7}$ km	See Sect. 5.1
	Volume equiv. radius	$124.8^{+3.0}_{-2.3}$ km	See Sect. 5.1

The observation on 2017 April 09 and on 2017 July 23 allowed us to probe C1R with a radial resolution of ~0.5 and ~1.0 km, respectively. This high resolution allowed the precise detection of W-shaped structures within C1R. In addition, there is a clear difference between the structures over the detections (see Fig. 11, which contains all resolved detections since 2014). From our observations we detect that the mean radial width of C1R is ~6.9 km and can range between ~4.8 and ~9.1 km.

The Danish 1.54-meter telescope in La Silla observed the event on 2017 July 23 in two different bands, visual (0.45–0.65 microns) and red (0.70–1.00 microns). There is no significant difference between these two observations, and we take this to mean that Chariklo's rings are mostly made of particles larger than a few microns.

The observations from the large telescope facilities on 2017 July 23 allowed for the first time a multi-chord detection of C2R. From this we can do an independent analysis of C2R and C1R and compare the obtained values. We obtained a 1σ agreement between the rings' pole orientation, a strong argument that they are coplanar, as expected. There is a slight difference between the centre position of both rings. That can be explained as a differential eccentricity between both rings, but this is not significant at the 3σ level. The determined radial difference in the ring plane between C1R and C2R is 14^{+7}_{-8} km. We checked for material between C1R and C2R and determined a 3σ upper limit of a ring material with normal opacity of 0.006.

Multiple stellar occultations between 2013 and 2020 combined with statistical analysis allowed the determination of Chariklo's 3D size and shape. We fitted 11 stellar occultations and determined that Chariklo is consistent with a triaxial ellipsoid with semi-axes of $143.8^{+1.4}_{-1.5}$, $135.2^{+1.4}_{-2.8}$, and $99.1^{+5.4}_{-2.7}$, and a volume equivalent radius of $124.8^{+3.0}_{-2.3}$. These values are consistent, within the error bars, with previous values derived from occultations (Leiva et al. 2017). We note that the new data, including multi-chord occultations, reduced the uncertainty on the modelled parameters. This 3D shape is essential for constraining the dynamics of Chariklo's ring system.

Stellar occultations provide Chariklo's astrometric positions at mas-level precision, even for single- or double-chord observations. These positions have been implemented in the NIMA software to update Chariklo's ephemeris. It has a propagated uncertainty of ~5 mas (~50 km at Chariklo's distance) up to January 2022. The 50 km uncertainty is small compared to Chariklo's diameter (~260 km) and the ring span (~800 km).

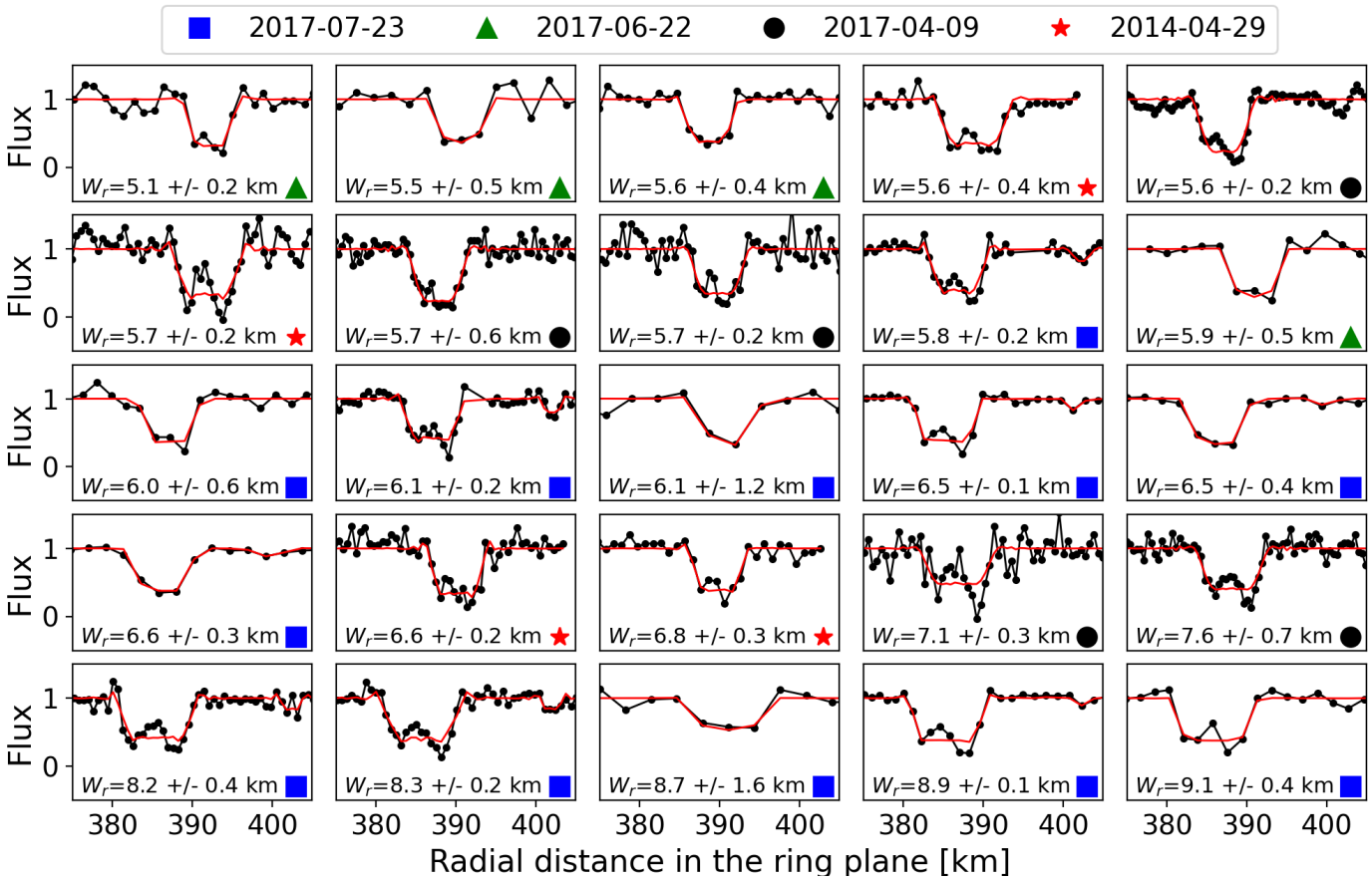

Fig. 11. All resolved detections of Chariklo C1R over radial distance in the ring plane. The black dots represent the observed flux and the red line is the best-fit model. The detections were sorted by radial width, as written in the lower part of each panel. The symbols in the lower right corners of the panels represent the different occultations. The data and analysis of the 2014 April 29 occultation was obtained from Bérard et al. (2017).

This permits a careful planning of future occultations with a high rate of success. In addition to the ephemerides of Chariklo, those of other small bodies with comparable accuracies are available on the Lucky Star webpage[8].

The parameters obtained in this work should be useful for constraining dynamical models of Chariklo and its rings, and should provide new insights into the formation and evolution of this system.

Acknowledgements. We would like to thank D. Souami for her useful feedback, which improved the quality of this manuscript. This work was carried out within the "Lucky Star" umbrella that agglomerates the efforts of the Paris, Granada and Rio teams, which is funded by the European Research Council under the European Community's H2020 (ERC Grant Agreement No. 669416). This research made use of SORA, a python package for stellar occultations reduction and analysis, developed with the support of ERC Lucky Star and LIneA/Brazil, within the collaboration Rio-Paris-Granada teams. This work has made use of data from the European Space Agency (ESA) mission *Gaia* (https://www.cosmos.esa.int/gaia), processed by the *Gaia* Data Processing and Analysis Consortium (DPAC, https://www.cosmos.esa.int/web/gaia/dpac/consortium). Part of this research is suported by INCT do e-Universo, Brazil (CNPQ grants 465376/2014-2). Based in part on observations made at the Laboratório Nacional de Astrofísica (LNA), Itajubá-MG, Brazil. The data include observations taken by the MiNDSTEp team at the Danish 1.54 m telescope at ESO's La Silla observatory" and "UGJ acknowledges funding from the European Union H2020-MSCA-ITN-2019 under grant no. 860470 (CHAMELEON) and from the Novo Nordisk Foundation Interdisciplinary Synergy Programme grant no. NNF19OC0057374. TRAPPIST-South is funded by the Belgian Fund for Scientific Research (Fond National de la Recherche Scientifique, FNRS) under the grant PDR T.0120.21. The authors acknowledge the use of Sonja Itting-Enke's C14 telescope and the facilities at the Cuno Hoffmeister Memorial Observatory (CHMO). The following authors acknowledge the respective CNPq grants: BEM 150612/2020-6; FB-R 314772/2020-0; RV-M 304544/2017-f5, 401903/2016-8; JIBC 308150/2016-3 and 305917/2019-6; MA 427700/2018-3, 310683/2017-3, 473002/2013-2. G.B.R. acknowledges CAPES-FAPERJ/PAPDRJ grant E26/203.173/2016 and CAPES-PRINT/UNESP grant 88887.571156/2020-00, MA FAPERJ grant E-26/111.488/2013 and ARGJr FAPESP grant 2018/11239-8. J.L.O., P.S.-S., R.D., and N.M. acknowledge financial support from the State Agency for Research of the Spanish MCIU through the "Center of Excellence Severo Ochoa" award to the Instituto de Astrofísica de Andalucía (SEV-2017-0709), from Spanish project AYA2017-89637-R, and from FEDER. P.S.-S. acknowledges financial support by the Spanish grant AYA-RTI2018-098657-J-I00 "LEO-SBNAF" (MCIU/AEI/FEDER, UE). E. Jehin is a Belgian FNRS Senior Research Associate. R.S. and O.C.W. acknowledge FAPESP grant 2016/24561-0 and CNPq grant 305210/2018-1. T.C.H. acknowledges financial support from the National Research Foundation (NRF; No. 2019R1I1A1A01059609).

[8] https://lesia.obspm.fr/lucky-star/predictions.php

References

Altenhoff, W. J., Menten, K. M., & Bertoldi, F. 2001, A&A, 366, L9
Anderson, B. 2019, J. Occul. Astron., 9, 9
Araujo, R. A. N., Winter, O. C., & Sfair, R. 2018, MNRAS, 479, 4770
Archinal, B. A., Acton, C. H., A'Hearn, M. F., et al. 2018, Celest. Mech. Dyn. Astron., 130, 22
Assafin, M., Vieira Martins, R., Camargo, J. I. B., et al. 2011, in *Gaia* follow-up network for the solar system objects : *Gaia* FUN-SSO workshop proceedings, 85
Assafin, M., Camargo, J. I. B., Vieira Martins, R., et al. 2012, A&A, 541, A142
Astropy Collaboration (Robitaille, T. P., et al.) 2013, A&A, 558, A33
Bauer, J. M., Grav, T., Blauvelt, E., et al. 2013, ApJ, 773, 22
Bérard, D., Sicardy, B., Camargo, J. I. B., et al. 2017, AJ, 154, 144
Braga-Ribas, F., Sicardy, B., Ortiz, J. L., et al. 2013, ApJ, 773, 26

Braga-Ribas, F., Sicardy, B., Ortiz, J. L., et al. 2014, Nature, 508, 72
Butcher, H., & Stevens, R. 1981, Kitt Peak National Observatory Newsletter, 16, 6
Butkevich, A. G., & Lindegren, L. 2014, A&A, 570, A62
Camargo, J. I. B., Vieira-Martins, R., Assafin, M., et al. 2014, A&A, 561, A37
Campins, H., & Fernández, Y. 2002, Earth Moon Planets, 89, 117
Cuzzi, J. N., Filacchione, G., & Marouf, E. A. 2018, The Rings of Saturn (London: Vintage Books), 51
Davies, J. K., McBride, N., Ellison, S. L., Green, S. F., & Ballantyne, D. R. 1998, Icarus, 134, 213
Desmars, J., Camargo, J. I. B., Braga-Ribas, F., et al. 2015, A&A, 584, A96
Desmars, J., Camargo, J., Berard, D., et al. 2017, AAS/Div. Planet. Sci. Meeting Abs., 49, 216.03
Desmars, J., Meza, E., Sicardy, B., et al. 2019, A&A, 625, A43
Duffard, R., Pinilla-Alonso, N., Ortiz, J. L., et al. 2014, A&A, 568, A79
Elliot, J. L., French, R. G., Meech, K. J., & Elias, J. H. 1984, AJ, 89, 1587
Esposito, L. W., Brahic, A., Burns, J. A., & Marouf, E. A. 1991, Particle properties and processes in Uranus' rings., eds. J. T. Bergstralh, E. D. Miner, & M. S. Matthews, 410
Fernández-Valenzuela, E., Ortiz, J. L., Duffard, R., Morales, N., & Santos-Sanz, P. 2017, MNRAS, 466, 4147
Fornasier, S., Lellouch, E., Müller, T., et al. 2013, A&A, 555, A15
Fornasier, S., Lazzaro, D., Alvarez-Candal, A., et al. 2014, A&A, 568, L11
French, R. G., Elliot, J. L., & Levine, S. E. 1986, Icarus, 67, 134
French, R. G., Nicholson, P. D., Porco, C. C., & Marouf, E. A. 1991, Dynamics and Structure of the Uranian Rings, eds. J. T. Bergstralh, E. D. Miner, & M. S. Matthews, 327
Gaia Collaboration (Brown, A. G. A., et al.) 2016a, A&A, 595, A2
Gaia Collaboration (Prusti, T., et al.) 2016b, A&A, 595, A1
Gaia Collaboration (Brown, A. G. A., et al.) 2018, A&A, 616, A1
Gaia Collaboration (Brown, A. G. A., et al.) 2021, A&A, 649, A1
Galiazzo, M., de la Fuente Marcos, C., de la Fuente Marcos, R., et al. 2016, Ap&SS, 361, 212
Herald, D., Gault, D., Anderson, R., et al. 2020, MNRAS, 499, 4570
Hyodo, R., Charnoz, S., Genda, H., & Ohtsuki, K. 2016, ApJ, 828, L8
Jewitt, D., & Kalas, P. 1998, ApJ, 499, L103
Leiva, R., Sicardy, B., Camargo, J. I. B., et al. 2017, AJ, 154, 159
Lellouch, E., Moreno, R., Müller, T., et al. 2017, A&A, 608, A45
Melita, M. D., Duffard, R., Ortiz, J. L., & Campo-Bagatin, A. 2017, A&A, 602, A27
Michikoshi, S., & Kokubo, E. 2017, ApJ, 837, L13
Nicholson, P. D., De Pater, I., French, R. G., & Showalter, M. R. 2018, The Rings of Uranus, eds. M. S. Tiscareno, & C. D. Murray (USA: Stewart Bruce), 93
Ortiz, J. L., Duffard, R., Pinilla-Alonso, N., et al. 2015, A&A, 576, A18
Ortiz, J. L., Santos-Sanz, P., Sicardy, B., et al. 2017, Nature, 550, 219
Pan, M., & Wu, Y. 2016, ApJ, 821, 18
Pavlov, H. 2020, Astrophysics Source Code Library [record ascl:2004.002]
Peixinho, N., Lacerda, P., Ortiz, J. L., et al. 2001, A&A, 371, 753
Rommel, F. L., Braga-Ribas, F., Desmars, J., et al. 2020, A&A, 644, A40
Sekiguchi, T., Ootsubo, T., Hasegawa, S., et al. 2012, IAU Symp. 1667, 6477
Sicardy, B., Ortiz, J. L., Assafin, M., et al. 2011, Nature, 478, 493
Sicardy, B., Buie, M. W., Benedetti-Rossi, G., et al. 2015, AAS/Div. Planet. Sci. Meeting Abs., 47, 104.01
Sicardy, B., El Moutamid, M., Quillen, A. C., et al. 2018, Planetary Ring Systems, Rings Beyond the Giant Planets, eds. M. S. Tiscareno, & C. D. Murray (Berlin: Springer), 135
Sicardy, B., Leiva, R., Renner, S., et al. 2019, Nat. Astron., 3, 146
Sickafoose, A. A., Bosh, A. S., Emery, J. P., et al. 2020, MNRAS, 491, 3643
Skottfelt, J., Bramich, D. M., Hundertmark, M., et al. 2015, A&A, 574, A54
Souami, D., Braga-Ribas, F., Sicardy, B., et al. 2020, A&A, 643, A125
Tancredi, G., & Favre, S. 2008, Icarus, 195, 851
Ticha, J., Tichy, M., Moravec, Z., et al. 1997, Minor Planet Electronic Circulars (USA: IAU Symposium), D11

[1] LESIA, Observatoire de Paris, Université PSL, CNRS, Sorbonne Université, Univ. Paris Diderot, Sorbonne Paris Cité, 5 place Jules Janssen, 92195 Meudon, France
e-mail: morgado.fis@gmail.com
[2] Laboratório Interinstitucional de e-Astronomia - LIneA, Rua Gal. José Cristino 77, Rio de Janeiro, 20921-400, Brazil
[3] Observatório Nacional/MCTI, R. General José Cristino 77, CEP 20921-400 Rio de Janeiro - RJ, Brazil
[4] Federal University of Technology - Paraná (UTFPR / DAFIS), Rua Sete de Setembro, 3165, CEP 80230-901, Curitiba, PR, Brazil
[5] Institut Polytechnique des Sciences Avancées IPSA, 63 boulevard de Brandebourg, 94200 Ivry-sur-Seine, France
[6] Institut de Mécanique Céleste et de Calcul des Éphémérides, IMCCE, Observatoire de Paris, PSL Research University, CNRS, Sorbonne Universités, UPMC Univ Paris 06, Univ. Lille, 77, Av. Denfert-Rochereau, 75014 Paris, France
[7] UNESP - São Paulo State University, Grupo de Dinâmica Orbital e Planetologia, CEP 12516-410, Guaratinguetá, SP, Brazil
[8] Université Côte d'Azur, Observatoire de la Côte d'Azur, CNRS, Laboratoire Lagrange, Bd de l'Observatoire, CS 34229, 06304 Nice Cedex 4, France
[9] Departamento de Astronomía, Universidad de Chile, Camino del Observatorio 1515, Las Condes, Santiago, Chile
[10] Instituto de Astrofísica de Andalucía, IAA-CSIC, Glorieta de la Astronomía s/n, 18008 Granada, Spain
[11] Universidade Federal do Rio de Janeiro - Observatório do Valongo, Ladeira Pedro Antônio 43, CEP 20.080-090 Rio de Janeiro - RJ, Brazil
[12] International Occultation Timing Association / European Section, Am Brombeerhag 13, 30459 Hannover, Germany
[13] Internationale Amateursternwarte e.V. (IAS), Mittelstrasse 6, 15749 Mittenwalde, Germany
[14] Institute for Astronomy, University of Edinburgh, Royal Observatory, Edinburgh EH9 3HJ, UK
[15] Florida Space Institute, University of Central Florida, 12354 Research Parkway, Partnership 1, Orlando, FL, USA
[16] BRAMON–Brazilian Meteor Observation Network, Nhandeara, Brazil
[17] Grupo de Matemática Aplicada e Processamento de Sinais, State University of Mato Grosso do Sul - UEMS, Cassilândia, CEP 79540-000, MS, Brazil
[18] IATE-OAC, Universidad Nacional de Córdoba-CONICET, Laprida 854, X5000 BGR, Córdoba, Argentina
[19] Department of Physics, Chemistry and Material Science, University of Namibia, Private Bag 13301, Windhoek, Namibia
[20] Centre for Space Research, North-West University, Potchefstroom 2520, South Africa
[21] Association T60, Observatoire Midi-Pyrénées, 14 avenue Edouard Belin, 31400 Toulouse, France
[22] Southwest Research Institute, 1050 Walnut Street, Suite 300, Boulder, CO 80302, USA
[23] Dogsheaven Observatory, SMPW Q25 CJ1 LT10B Brasilia, Brazil
[24] Association of Argentine Observatories of Minor Bodies (AOACM)), Argentina
[25] Centro de Astronomía (CITEVA), Universidad de Antofagasta, Av. Angamos 601, Antofagasta, Chile
[26] Ciel & Espace, Paris, France
[27] University of St Andrews, Centre for Exoplanet Science, SUPA School of Physics & Astronomy, North Haugh, St Andrews, KY16 9SS, UK
[28] Universidade Estadual de Ponta Grossa (UEPG), Ponta Grossa, Brazil
[29] Summit Kinetics Inc, USA
[30] Panamanian Observatory in San Pedro de Atacama - OPSPA, San Pedro de Atacama, Chile
[31] Department of Physics, Southern University of Science and Technology, Shenzhen 518055, PR China
[32] Centro Brasileiro de Pesquisas Físicas, Rua Dr Xavier Sigaud 150, Rio de Janeiro 22290-180, Brazil
[33] Trans-Tasman Occultation Alliance (TTOA), Wellington PO Box 3181, New Zealand
[34] Association Réunionnaise pour l'Etude du Ciel Austral - ARECA, Sainte-Marie, La Réunion, France
[35] Institute of Astronomy, Faculty of Physics, Astronomy and Informatics, Nicolaus Copernicus University, Grudziadzka 5, 87-100, Torun, Poland
[36] Department of Astronomy and Space Science, Chungnam National University, 34134 Daejeon, Republic of Korea
[37] Observatório SONEAR, Oliveira, Brazil

[38] STAR Institute, Université de Liège, Allée du 6 août, 19C, 4000 Liège, Belgium
[39] Centre for ExoLife Sciences (CELS), Niels Bohr Institute, øster Voldgade 5, 1350 Copenhagen, Denmark
[40] Astronomical Association of Queensland, 5 Curtis Street, Pimpama QLD 4209, Australia
[41] Department of Physics and Astronomy, University of North Carolina, Chapel Hill, USA
[42] Central (Pulkovo) Observatory of the Russian Academy of Sciences, 196140, 65/1 Pulkovskoye Ave., Saint Petersburg, Russia
[43] Lowell Observatory, 1400 W Mars Hill Road, Flagstaff, AZ 86001, USA
[44] Massachusetts Institute of Technology, Department of Earth, Atmospheric and Planetary Sciences, 77 Massachusetts Avenue, Cambridge, MA 02139, USA
[45] The Astronomical Research Institute, Ashmore, IL, UK
[46] International Occultation Timing Association (IOTA), PO Box 7152, WA, 98042, USA
[47] NASA Johnson Space Center Astronomical Society, Houston, TX, USA
[48] Universidade Estadual do Oeste do Paraná (Unioeste), Avenida Tarquínio Joslin dos Santos 1300, Foz do Iguaçu, PR, 85870-650, Brazil
[49] Polo Astronômico Casimiro Montenegro Filho/FPTI-BR, Avenida Tancredo Neves 6731, Foz do Iguaçu, PR, 85867-900, Brazil
[50] San Pedro de Atacama Celestial Explorations - SPACE, Chile
[51] Comisión Nacional de Investigación y Desarrollo Aeroespacial del Perú - CONIDA, Luis Felipe Villarán 1069, San Isidro, Lima, Peru
[52] Observatorio Astronómico de Moquegua, CP Cambrune, Carumas, Moquegua, Peru
[53] Physics and Astronomy Department, Appalachian State University, Boone, NC 28608, USA
[54] Astrocan Clube de Astronomia Nhandeara, Nhandeara, Brazil
[55] Centre for mathematical Plasma Astrophysics, Department of Mathematics, KU Leuven, Celestijnenlaan 200B, 3001 Leuven, Belgium
[56] Centre for Electronic Imaging, Department of Physical Sciences, The Open University, Milton Keynes, MK7 6AA, UK
[57] Association Des Étoiles pour Tous, 19 Rue Saint Laurent, Maisoncelles, 77320 Saint Martin du Boschet, France
[58] Observatorio Astronómico Córdoba UNC, Laprida 854, Córdoba, Argentina
[59] AGORA observatoire des Makes, AGORA, 18 Rue Georges Bizet, Observatoire des Makes, 97421 La Rivière, France
[60] Institute of Astrophysics, Pontificia Universidad Catolica de Chile, Av. Vicuña Mackenna 4860, Santiago, Chile
[61] Millennium Institute of Astrophysics, Chile
[62] Centre of Astro-Engineering, Pontificia Universidad Catolica de Chile, Av. Vicuña Mackenna 4860, Santiago, Chile
[63] Department of Electrical Engineering, Pontificia Universidad Catolica de Chile, Av. Vicuña Mackenna 4860, Santiago, Chile

Appendix A: Observational circumstances

Table A.1 summarises the observational circumstances of each station for the eight stellar occultations presented here (name of station, coordinates, observers, telescope aperture, detector, band, exposure and cycle times, and the light curve root mean square (RMS) noise. The status of each observation is mentioned (positive or negative detection of the main body, resolved, unresolved, or no detection of the rings). Weather overcast and instrumental issues are also indicated.

Appendix B: Occultation maps

Figures B.1, B.2, B.3, B.4, B.5, B.6, B.7, and B.8 contain the occultation maps for the eight unpublished stellar occultations between 2017 and 2020. The maps are organised in inverse chronological order. The blue dots stand for the stations with a positive detection over the main body, the green dots are those with positive detections only for the rings, the yellow dots are stations with data that was unfit to detect the rings and negatives for the main body, and the red dots are stations without data covering the occultation instants (weather overcast or instrumental issues). The black dots stand for the centre of Chariklo every minute, and the big black dot represents the closest approach time. The solid black line stands for the path of Chariklo's shadow and the dashed line for the ring's shadow.

Appendix C: Occultation times and fitted parameters

Table C.1 lists the fitted times (immersion and emersion), duration of the event (Δt), apparent opacity (p', in sky plane), and minimum χ^2 per degree of freedom (χ^2_{pdf}) obtained for all the positive detections. The events are presented in reverse chronological order, and the detections are listed from northernmost to southernmost stations. The type of detection is mentioned: MB for Chariklo's main body; C1R and C2R for ring detections, usually flagged as 1st and 2nd (immersion and emersion, respectively).

Table C.2 presents the ring parameters projected into the ring plane for each detection: the radial distance (r) to the ring centre (assumed to be circular), the radial width (W_r), normal opacity (p_N), and equivalent width (E_p). The number of data points within each detection (#) is also given, as well as the S/N of the observed stellar drops, which is the ratio of the stellar drop (one minus the bottom flux of the event, ϕ_0) to the RMS noise of the light curve.

Appendix D: Chariklo's updated positions

Stellar occultations provide precise astrometric position of the occulting body relative to the occulted star. If a new and more accurate position of the star is available, we can update the object's position (Rommel et al. 2020). Table 5 provides the solutions derived from seven stellar occultations observed between 2017 and 2020, using the Gaia Early Data Release 3 (GEDR3). Here we also update results obtained from 12 occultations between 2013 and 2016 (Braga-Ribas et al. 2014; Bérard et al. 2017), using again the GEDR3.

Desmars et al. (2017) updated the positions obtained from pre-2017 events using the GDR2 catalogue. We use Chariklo's previous position (α_c, δ_c), and the GDR2 star position ($\alpha_{GDR2}, \delta_{GDR2}$) and the GEDR3 ($\alpha_{GEDR3}, \delta_{GEDR3}$), both at epoch. The updated Chariklo position (α'_c, δ'_c) is thus obtained from

$$\alpha'_c = \alpha_c + \alpha_{GEDR3} - \alpha_{GDR2}, \quad \text{(D.1)}$$

$$\delta'_c = \delta_c + \delta_{GEDR3} - \delta_{GDR2}. \quad \text{(D.2)}$$

The updated Chariklo positions between 2013 and 2017 are given in Table D.1.

Appendix E: The case of the 2019 September 04 event in Hawaii

On 2019 September 04, Chariklo's system occulted a mag G 13.586 star as seen from Hawaii. A run was triggered to observe the event from the 8.1 m Gemini North telescope in Mauna Kea. Unfortunately, the weather only allowed the observations to start a few minutes after the occultation, as can be seen in Figure E.1.

A simultaneous observation was set up at Mauna Loa, using a 0.36 m portable telescope. Due to a technical failure, the images were not recorded, but were being displayed on screen. The observers were able to use a smartphone to film the notebook screen, with the GPS time inserted in each frame (see Figure E.2).

As the smartphone video recording started after the occultation by the main body, only a transit of C1R in front of the star was recorded. This atypical dataset was analysed using the aperture photometry package of `PyMovie` (Anderson 2019), resulting in the light curve shown in Figure E.3. As we could not retrieve the exact mid-time for each frame, we determined the immersion time using the time stamped in the images right before and after the star's disappearance. We then considered that the mean time between the images with and without the star provides the immersion time, with an uncertainty of half the time between these two frames. The same protocol was followed to determine the emersion time.

The mid-time of the C1R occultation is thus evaluated at UTC 08:02:38.993±0.017 s. The NIMA v.18 Chariklo's ephemeris having an uncertainty of 20 km for this event, this mid-time corresponds to a (f, g) position in the sky plane of (250.945 ± 20.0, −36.121 ± 20.0) km. The radial width of CR1 in the ring plane is then 6.77 ± 0.53 km, with normal opacity of 0.370 ± 0.094. These results are consistent with the obtained parameters from other occultations. If more observations of this event were to be obtained by other teams, the data presented here could be used to better constrain the geometry of this occultation.

Appendix F: Light curves

This section provides the plots of the normalised light curves versus UTC analysed in this work. There are 40 light curves obtained during the seven occultations observed between 2017 and 2020 (excluding the 2019 September 04 event). The events are listed in inverse chronological order, and the light curves are plotted from the northernmost to the southernmost stations. The date, event, and observer are indicated in the title and label of each figure. The upper panel contains the complete normalised light curve (black dots) and the fitted model (red line). The bottom panels contain zoomed-in views of a few seconds each centred on the detections of C1R, and the immersions and emersions behind the main body, when detected.

Table A.1. Observational stations, technical details, and circumstance.

Site Status Main Body Status Ring	Longitude Latitude Altitude	Observers	Telescope aperture Detector Filter	Exposure Time Cycle (s)	Light curve RMS (flux)
2020-06-19 – Australia					
Glenlee	150^o 30' 01.6" E	S. Kerr	30 cm	0.640	0.138
Positive Detection	23^o 16' 10.1" S		Watec 910BD	0.640	
Unresolved Detection	50 m		Clear		
2019-09-04 – Hawaii					
Gemini North – Mauna Kea	155^o 28' 08.0" W	F. Braga-Ribas	810 cm	0.040	0.019
Instrumental Issue	19^o 49' 25.0" N		Andor/IXon-EM	0.040	
	4184 m		Blue-g / Red-i		
Mauna Loa	155^o 34' 34.9" W	P. Maley	36 cm	0.017	0.127
Instrumental Issue	19^o 32' 10.6" N	C. Erickson	Watec 910HX	0.017	
Resolved Detection[a]	3395 m		Clear		
2019-08-08 – La Réunion / Namibia					
Ste. Marie / La Réunion	55^o 34' 00.2" E	B. Mondon	28 cm	0.500	0.269
Positive Detection	20^o 53' 48.5" S		QHY174M	0.500	
No Detection[b]	50 m		Clear		
Ste. Marie / La Réunion	55^o 31' 08.6" E	G. Hesler	40 cm	0.500	0.405
Positive Detection	20^o 54' 38.9" S		QHY174M	0.500	
No Detection	85 m		Clear		
Maido / La Réunion	55^o 23' 14.5" E	T. Payet	30 cm	0.500	0.286
Positive Detection	21^o 04' 15.5" S		ASI178MM	0.500	
No Detection	2195 m		Clear		
Les Makes / La Réunion	55^o 24' 36.3" E	P. Thierry	60 cm	0.531	0.263
Positive Detection	21^o 11' 56.1" S		ASI178MM	0.531	
No Detection	990 m		Clear		
Langevin / La Réunion	55^o 38' 47.7" E	F. Colas	28 cm	0.333	0.290
Positive Detection	21^o 23' 12.0" S		ASI178MM	0.333	
No Detection	20 m		Clear		
Vastrap Guestfarm / Namibia	27^o 44' 05.2" E	M. Kretlow	40 cm	—	—
Instrumental Issue	18^o 25' 49.5" S		Merlin/Raptor	—	
	1090 m		Clear		
2019-08-02 – Australia					
Yass	148^o 58' 35.1" E	W. Hanna	51 cm	3.000	0.207
Positive Detection	34^o 51' 50.9" S		QHY174GPS	3.001	
No Detection	536 m		Clear		
Murrumbateman	148^o 59' 54.8" E	D. Herald	40 cm	1.280	0.204
Positive Detection	34^o 57' 31.5" S		Watec 910BD	1.280	
No Detection	594 m		Clear		
Flynn	149^o 02' 57.5" E	J. Newman	40 cm	1.280	0.532
No Detection	35^o 11' 55.3" S		Watec 910BD	1.280	
No Detection	657 m		Clear		
2017-08-24 – Brazil					
OPD – Brazópolis	45^o 34' 57.5" W	J. I. B. Camargo	160 cm	0.500	0.063
Positive Detection	22^o 32' 07.8" S	F. Quispe-Huaynasi	Andor/IXon-EM	0.513	
Unresolved Detection	1864 m		Clear		

[a] Due to instrumental issues the original dataset was lost; however, a video recorded by the observer's smartphone was used to derive the immersion and emersion times of the second detection of the ring.

[b] No detection means that the dataset's features do not allow the detection of Chariklo's rings.

Table A.1. [Cont.] Observational stations, technical details, and circumstance.

Site Status Main Body Status Ring	Longitude Latitude Altitude	Observers	Telescope aperture Detector Filter	Exposure Time Cycle (s)	Light curve RMS (flux)
2017-07-23 – South America					
San Pedro de Atacama / Chile Negative Detection No Detection	68^o 10' 44.0" W 22^o 57' 14.0" S 2397 m	N. Morales	41 cm SBIG STL11K3 Clear	2.000 4.370	0.058
San Pedro de Atacama / Chile Negative Detection Unresolved Detection	68^o 10' 48.0" W 22^o 57' 09.0" S 2396 m	J. Fabrega	40 cm FLI PL16803 Clear	1.000 2.700	0.099
San Pedro de Atacama / Chile Negative Detection No Detection	68^o 10' 48.0" W 22^o 57' 09.0" S 2396 m	J. F. Soulier	40 cm QHY9 CCD Clear	3.000 7.000	0.023
San Pedro de Atacama / Chile Negative Detection No Detection	68^o 10' 48.0" W 22^o 57' 09.0" S 2396 m	A. Maury	50 cm FLI13803 Clear	3.000 5.650	0.045
Cerro Burek / Argentina Negative Detection No Detection	69^o 18' 25.0" W 31^o 47' 12.0" S 2665 m	N. Morales	45 cm SBIG STL11000 Clear	2.000 4.250	0.066
Ckoirama / Chile Negative Detection No Detection	69^o 55' 49.0" W 24^o 05' 21.0" S 0964 m	J. P. Colque	60 cm FLI PL16801 Clear	1.000 2.569	0.188
VLT – Cerro Paranal / Chile Negative Detection Resolved Detection	70^o 24' 16.5" W 24^o 37' 39.3" S 2635 m	B. Sicardy	820 cm HAWK-I K_s-band	0.100 0.100	0.027
SSO[c] – Cerro Paranal / Chile Negative Detection Unresolved Detection	70^o 24' 16.5" W 24^o 37' 39.3" S 2635 m	E. Jehin	100 cm Andor/IKONL g' / I + z	1.200 / 1.200 2.000 / 2.040	0.020 / 0.013
Tolar Grande / Argentina Negative Detection Resolved Detection	67^o 23' 43.6" W 24^o 35' 23.5" S 3524 m	M. Kretlow R. A. Artola	41 cm Merlin/Raptor Clear	0.130 0.130	0.092
Cono de Arita / Argentina Positive Detection No Detection	67^o 46' 00.2" W 25^o 01' 59.8" S 3532 m	M. D. Starck-Cuffini M. V. Sieyra	25 cm ASI178MM Clear	0.500 0.500	0.161
El Rodeo / Argentina Positive Detection Unresolved Detection	66^o 08' 35.4" W 24^o 52' 37.0" S 3022 m	E. Meza R. Melia	36 cm Merlin/Kite Clear	0.150 0.170	0.358
Cachi Adentro / Argentina Positive Detection No Detection	66^o 14' 16.7" W 25^o 05' 33.9" S 2684 m	E. M. Schneiter C. Colazo M. Buie	36 cm Merlin/Raptor Clear	0.100 0.100	0.452
Augusto de Lima / Brazil Positive Detection No Detection	44^o 04' 08.4" W 18^o 01' 20.7" S 0620 m	B. L. Giacchini G. Benedetti-Rossi	30 cm Merlin/Raptor Clear	1.000 1.000	0.174
El Salvador / Chile Positive Detection Unresolved Detection	69^o 45' 03.8" W 26^o 18' 48.3" S 1607 m	J-L. Dauvergne	28 cm Merlin/Raptor Clear	0.050 0.050	0.318
São José do Rio Preto / Brazil Positive Detection No Detection	49^o 17' 52.2" W 20^o 42' 43.4" S 0482 m	R. Sfair A. Amarante R. Poltronieri	35 cm Merlin/Raptor Clear	1.000 1.000	0.213
Inca de Oro / Chile Positive Detection Unresolved Detection	69^o 54' 45.6" W 26^o 44' 45.3" S 1592 m	S. Bouley	25 cm Merlin/Raptor Clear	0.100 0.100	0.267
Bilac / Brazil Positive Detection No Detection	50^o 30' 20.9" W 21^o 23' 38.6" S 0426 m	L. S. Amaral	25 cm Canon T1i Clear	6.000 11.000	0.150
Danish – La Silla / Chile Negative Detection Resolved Detection	70^o 44' 20.2" W 29^o 15' 21.3" S 2337 m	C. Snodgrass T. C. Hinse U. G. Jorgensen M. Dominik J. Skottfelt	154 cm Lucky Imager Visual & Red[d]	0.033 / 0.033 0.034 / 0.034	0.082 / 0.063

[c] The SSO observations were done at the telescopes Io and Europa.

[d] The Danish dual experiment observed in the visual (0.45-0.65 μm) and red (0.7-1.0 μm) bands.

Table A.1. [Cont.] Observational stations, technical details, and circumstance.

Site Status Main Body Status Ring	Longitude Latitude Altitude	Observers	Telescope aperture Detector Filter	Exposure Time Cycle (s)	Light curve RMS (flux)
2017-07-23 – South America [Cont.]					
1m – La Silla / Chile	70^o 44' 20.2" W	A. Zapata	100 cm	0.100	0.074
Negative Detection	29^o 15' 21.3" S	P. Torres	Merlin/Raptor	0.100	
Resolved Detection	2337 m		Clear		
TRAPPIST-South – La Silla / Chile	70^o 44' 20.2" W	E. Jehin	60 cm	2.000	0.040
Negative Detection	29^o 15' 21.3" S		FLI PL3041-BB	2.795	
Unresolved Detection	2337 m		Clear		
Foz do Iguaçu / Brazil	54^o 35' 37.0" W	D. I. Machado	28 cm	4.000	0.038
Negative Detection	25^o 26' 05.0" S	L. L. Trabuco	Merlin/Raptor	4.000	
No Detection	0184 m		Clear		
OPD – Brazõpolis / Brazil	45^o 34' 57.5" W	F. Braga-Ribas	160 cm	0.117	0.029
Negative Detection	22^o 32' 07.8" S	F. L. Rommel	Andor/IXon-EM	0.130	
Resolved Detection	1864 m		Clear		
SARA – Cerro Tololo / Chile	70^o 48' 23.0" W	R. Leiva	60 cm	1.000	0.094
Negative Detection	30^o 10' 11.0" S	S. Levine	FLI	1.679	
Resolved Detection	2207 m	C. Zuluaga	Clear		
PROMPT[e] – Cerro Tololo / Chile	70^o 48' 23.0" W	J. Pollock	40 cm	1.000	0.037
Negative Detection	30^o 10' 11.0" S	V. Kouprianov	AltaU-47	0.615	
Resolved Detection	2207 m	D. Reichart	Clear		
		T. Linder			
Oliveira / Brazil	43^o 59' 03.1" W	C. Jacques	45 cm	—	—
Weather Overcast	19^o 52' 55.0" S		ML FLI16803	—	
	982 m		Clear		
Guaratinguetá / Brazil	45^o 11' 25.0" W	T. Santana	40 cm	—	—
Weather Overcast	22^o 48' 34.0" S	T. Moura	Merlin/Raptor	—	
	0567 m	O. C. Winter	Clear		
		T. Akemi			
BrasÃlia / Brazil	47^o 54' 39.9" W	P. Cacella	50 cm	—	—
Weather Overcast	15^o 53' 29.9" S		ASI174MM	—	
	1064 m		Clear		
Ponta Grossa / Brazil	50^o 05' 56.6" W	C. L. Pereira	40 cm	—	—
Weather Overcast	25^o 05' 22.5" S	M. Emilio	Merlin/Raptor	—	
	910 m		Clear		
SOAR - Cerro Pachõn / Chile	70^o 44' 21.1" W	J. I. B. Camargo	410 cm	—	—
Weather Overcast	30^o 14' 16.9" S		Merlin/Raptor	—	
	2694 m		Clear		
2017-06-22 – Namibia					
Outeniqua Lodge	16^o 49' 17.7" E	F. Colas	25 cm	0.100	0.325
Positive Detection	21^o 17' 58.2" S	J. Desmars	Merlin/Raptor	0.100	
Unresolved Detection	1416 m		Clear		
Onduruquea Guest Farm	15^o 59' 33.7" E	M. Kretlow	50 cm	0.075	0.116
Positive Detection	21^o 36' 26.0" S		Merlin/Raptor	0.080	
Resolved Detection	1220 m		Clear		
Windhoek	17^o 06' 31.9" E	M. Backes	35 cm	0.150	0.148
Positive Detection	22^o 41' 55.2" S		Merlin/Raptor	0.150	
Unresolved Detection	1902 m		Clear		
Windhoek	17^o 06' 31.9" E	E. Meza	40 cm	0.200	0.151
Positive Detection	22^o 41' 55.2" S		ASI178MM	0.203	
Unresolved Detection	1902 m		Clear		
Tivoli Lodge	18^o 01' 01.2" E	L. Maquet	40 cm	0.075	0.175
Positive Detection	23^o 27' 40.2" S		Merlin/Raptor	0.075	
Unresolved Detection	1344 m		Clear		
Hakos	16^o 21' 41.3" E	W. Beisker	50 cm	0.050	0.122
Negative Detection	23^o 14' 11.0" S		Merlin/Raptor	0.050	
Resolved Detection	1843 m		Clear		

[e] The PROMPT observation were the combined data observed by P1, P3, and P5, allowing for a short cycle.

Table A.1. [Cont.] Observational stations, technical details, and circumstance.

Site Status Main Body Status Ring	Longitude Latitude Altitude	Observers	Telescope aperture Detector Filter	Exposure Time Cycle (s)	Light curve RMS (flux)
2017-04-09 – Namibia					
Wabi Lodge	17^o 32' 00.6" E	J. L. Dauvergne	30 cm	0.100	0.212
Positive Detection	20^o 20' 38.9" S		Merlin/Raptor	0.100	
Resolved Detection	1382 m		Clear		
Weaver Rocks Lodge	16^o 50' 29.9" E	M. Kretlow	50 cm	0.080	0.147
Positive Detection	20^o 41' 56.3" S		Merlin/Raptor	0.080	
Resolved Detection	1647 m		Clear		
Hakos	16^o 21' 42.0" E	K. L. Bath	50 cm	0.100	0.089
Negative Detection	23^o 14' 10.0" S		Merlin/Raptor	0.100	
Resolved Detection[f]	1881 m		Clear		

[f] Only the second detection of the C1R was observed, due to the weather conditions.

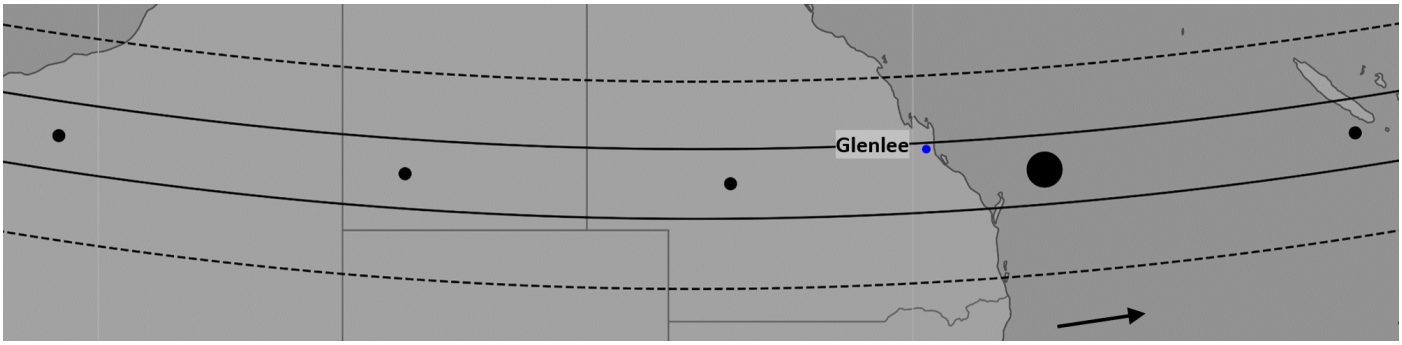

Fig. B.1. Occultation map for the 2020 June 19 event.

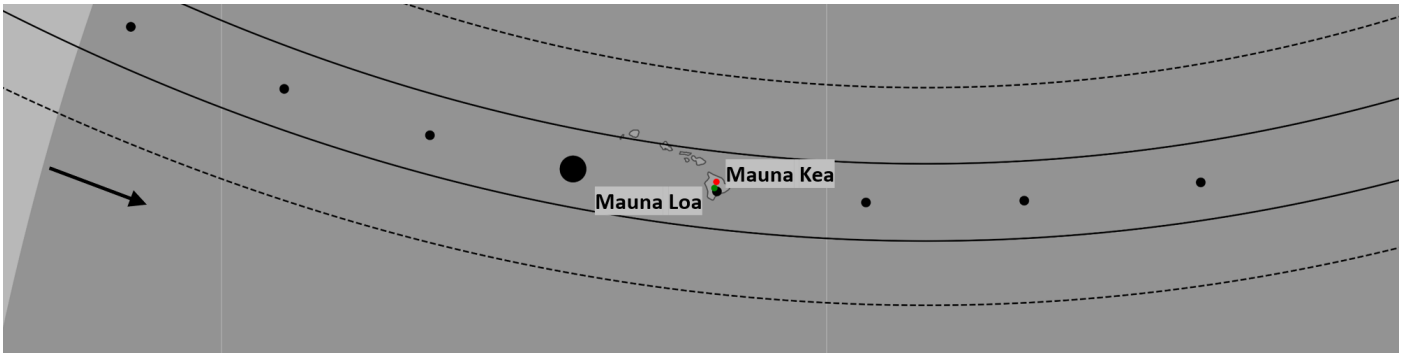

Fig. B.2. Occultation map for the 2019 September 04 event.

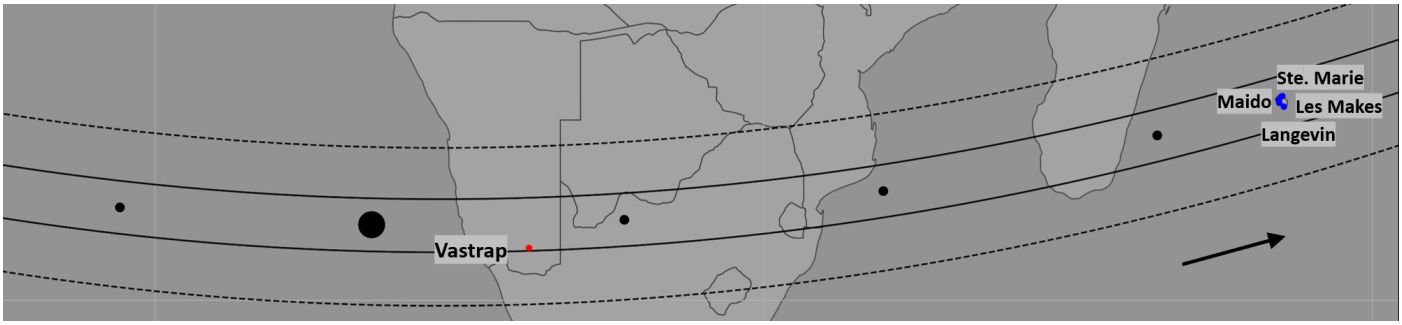

Fig. B.3. Occultation map for the 2019 August 08 event.

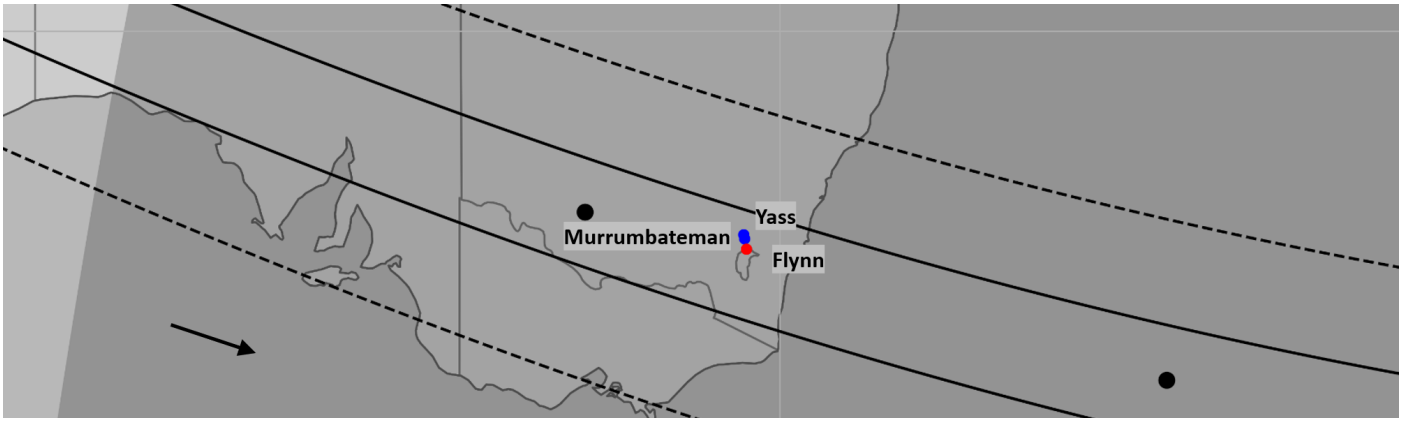

Fig. B.4. Occultation map for the 2019 August 02 event.

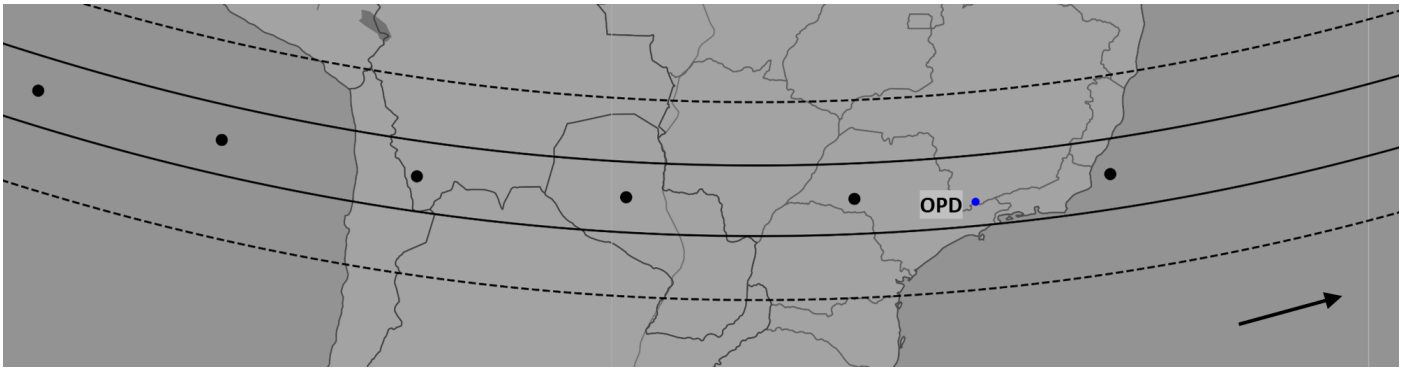

Fig. B.5. Occultation map for the 2017 August 24 event.

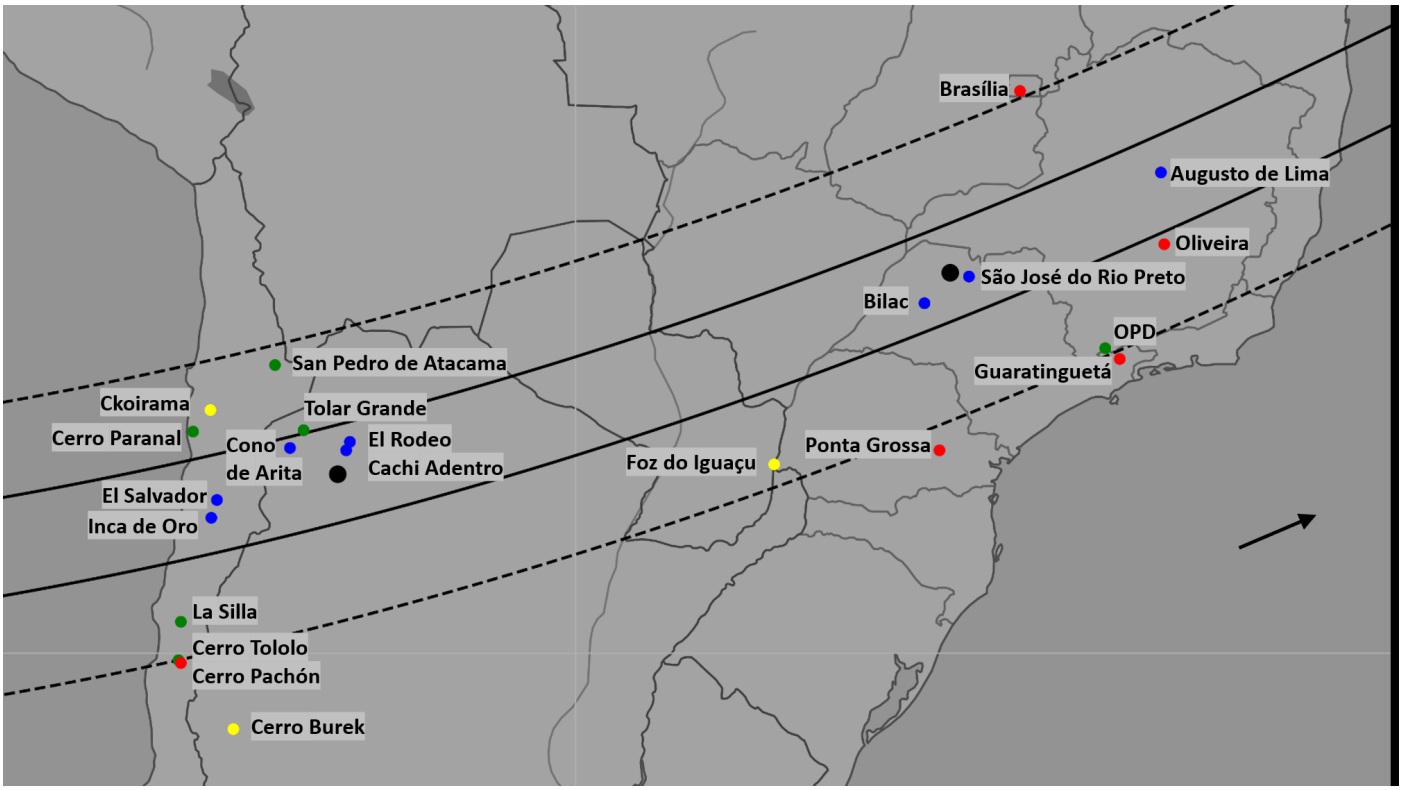

Fig. B.6. Occultation map for the 2017 July 23 event.

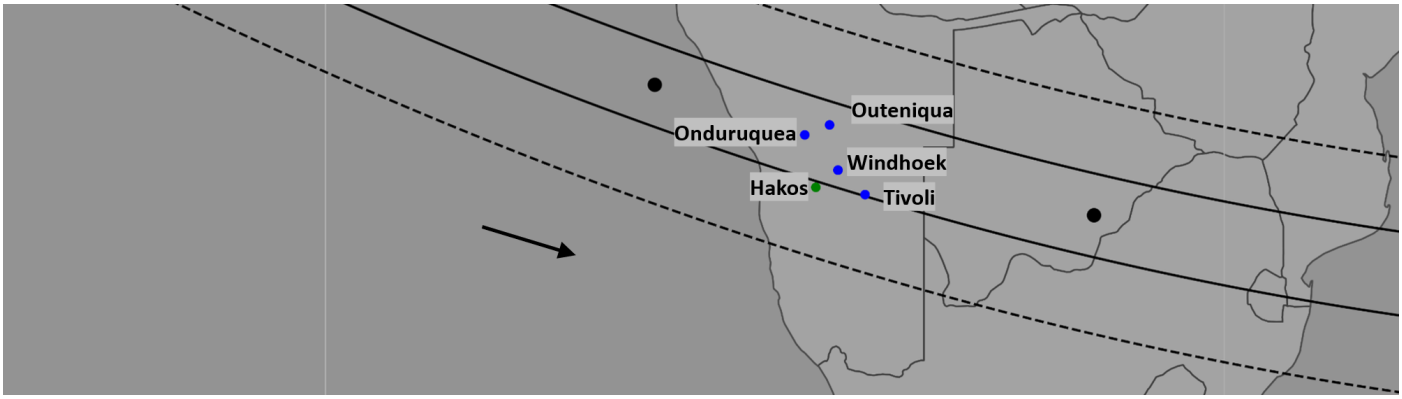

Fig. B.7. Occultation map for the 2017 June 22 event.

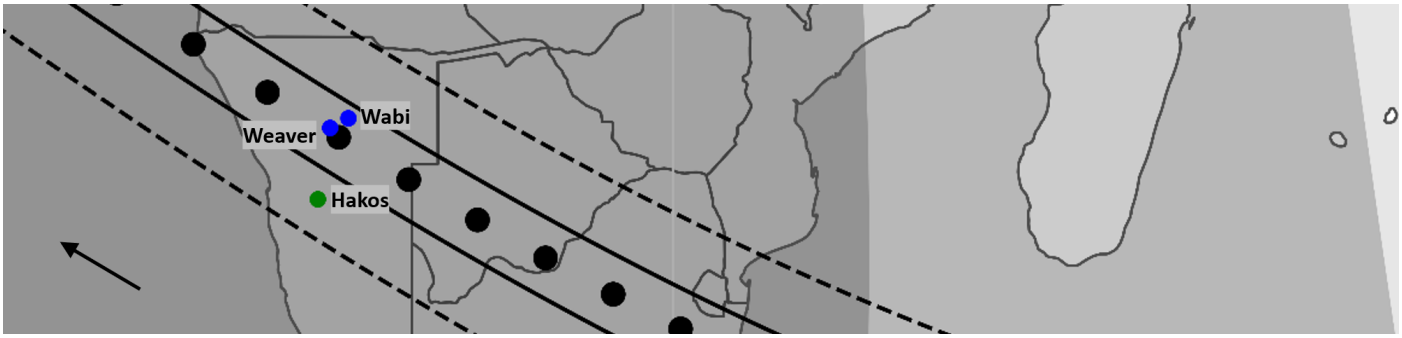

Fig. B.8. Occultation map for the 2019 September 04 event.

Table D.1. Update of astrometrical Chariklo positions for the events observed between 2013 and 2016.

Date and time UTC	Right Ascension	Declination
2013-06-03 06:25:30.000	16^h 56^m $06^s.5117522$	-40° 31' 30".107042
2014-02-16 07:45:35.000	17^h 35^m $55^s.2915296$	-38° 05' 17".300445
2014-03-16 20:31:45.000	17^h 40^m $39^s.8348967$	-38° 25' 46".483279
2014-04-29 23:14:12.000	17^h 39^m $02^s.1051292$	-38° 52' 48".749358
2014-06-28 22:24:35.000	17^h 24^m $50^s.3869110$	-38° 41' 05".485778
2015-04-26 02:11:58.000	18^h 10^m $46^s.1055222$	-36° 38' 56".597743
2015-05-12 17:55:40.000	18^h 08^m $29^s.3099452$	-36° 44' 56".801226
2016-07-26 00:00:00.000	18^h 20^m $35^s.3610788$	-34° 02' 29".041382
2016-08-10 14:23:00.000	18^h 17^m $47^s.3503443$	-33° 51' 02".478041
2016-08-10 16:43:00.000	18^h 17^m $46^s.4742139$	-33° 50' 57".707107
2016-08-15 11:38:00.000	18^h 17^m $06^s.2478821$	-33° 46' 56".499075
2016-10-01 10:10:00.000	18^h 16^m $20^s.0944710$	-33° 01' 10".842803

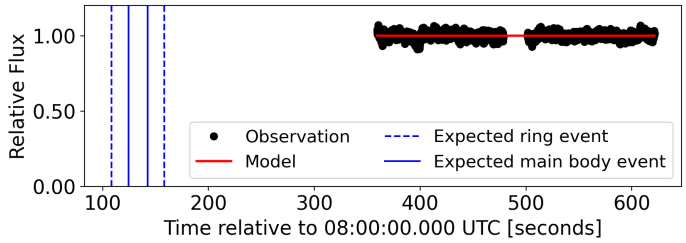

Fig. E.1. Light curve obtained at Gemini North on 2017 July 23. The solid blue vertical lines stand for the expected times for the main body occultation and the dashed lines for the expected times for the ring. The black points are the data points, which were taken in two blocks separated by a few seconds. See text for details.

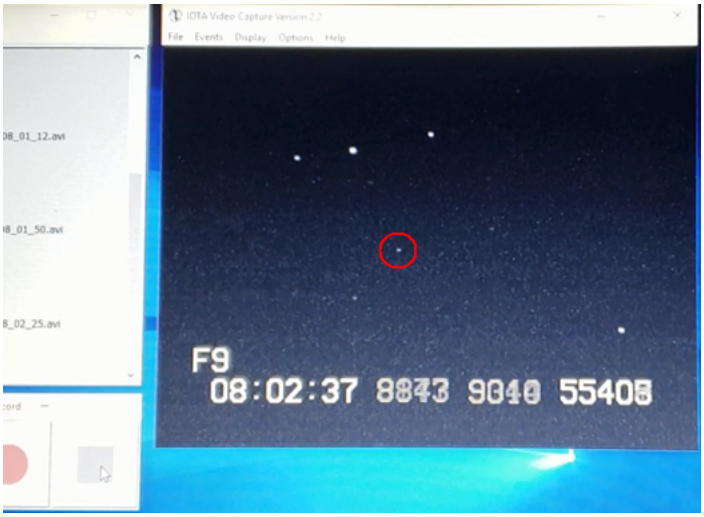

Fig. E.2. One frame from the smartphone video of the notebook screen, during the 2019 September 04 event. The occulted star is highlighted by the red circle.

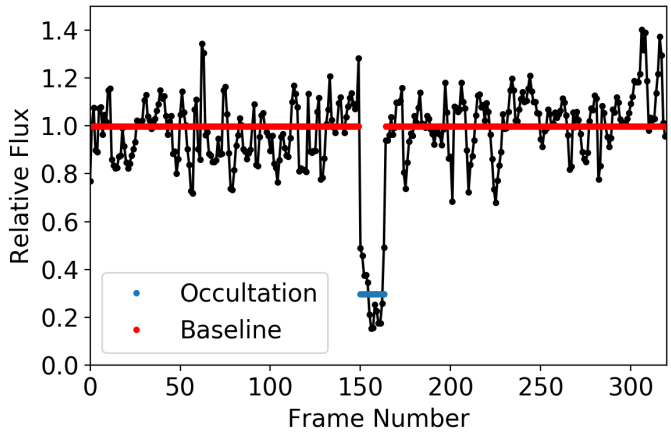

Fig. E.3. Normalised flux vs. frame number obtained at Mauna Loa during the 2019 September 04 event, showing the occultation by C1R. The red line stands for the baseline flux (1.0).

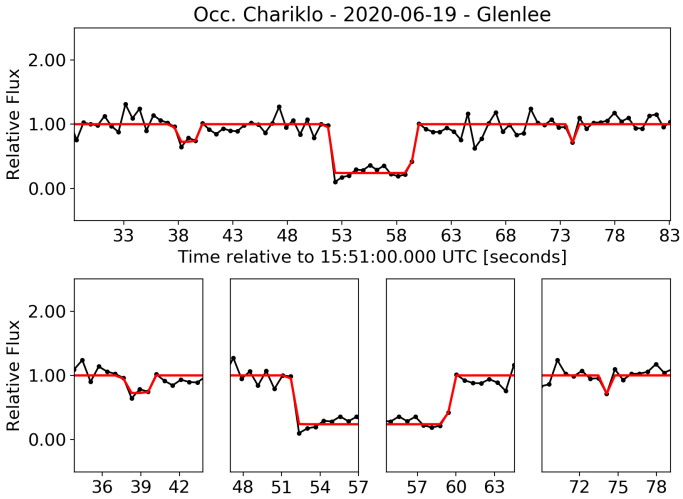

Fig. F.1. Light curve obtained in Glenlee on 2020 June 19. The event, date, and observer are indicated in the title and label. The upper panel contains the complete normalised light curve (black dots) and the fitted model (red line). The bottom panels contain zoomed-in views of a few seconds each centred on the detections of C1R, and the immersions and emersions behind the main body.

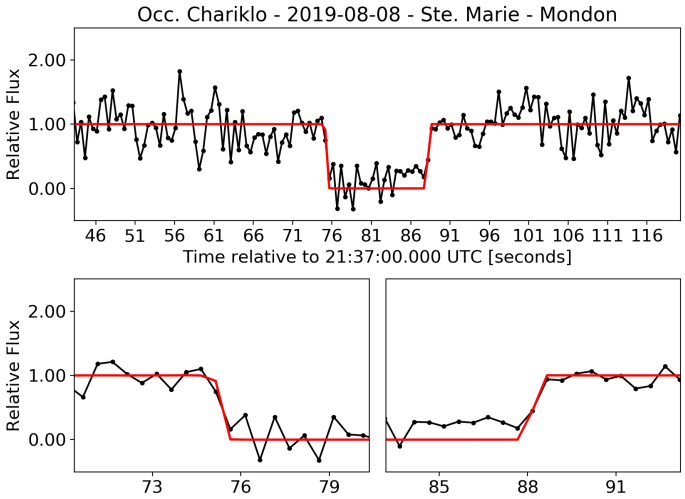

Fig. F.2. Light curve obtained at Ste. Marie by Mondon on 2019 August 08.

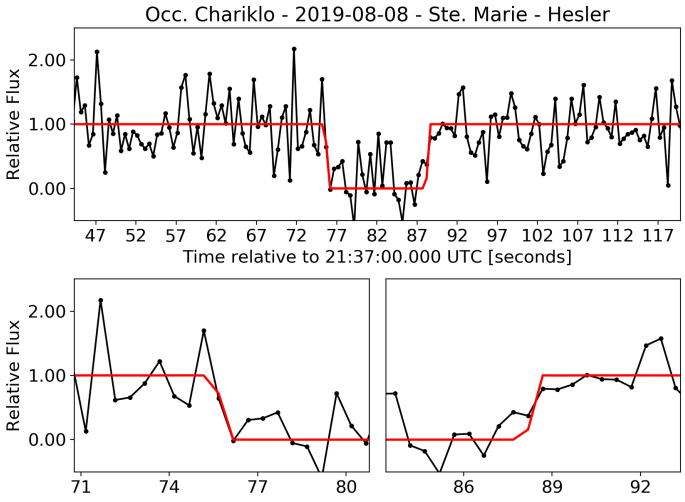

Fig. F.3. Light curve obtained at Ste. Marie by Hesler on 2019 August 08.

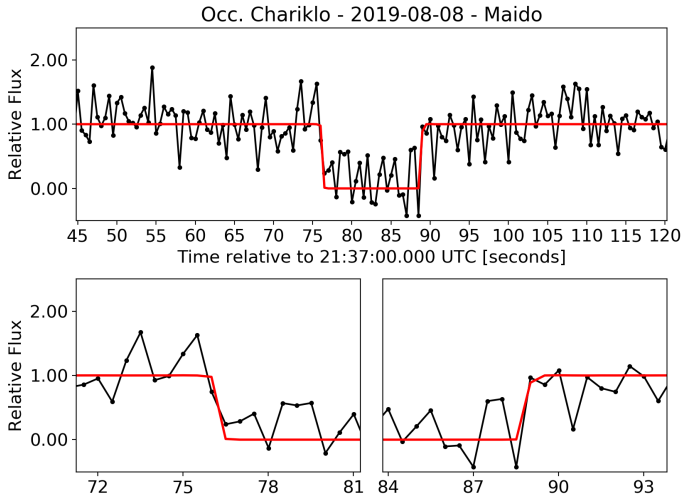

Fig. F.4. Light curve obtained at Maido on 2019 August 08.

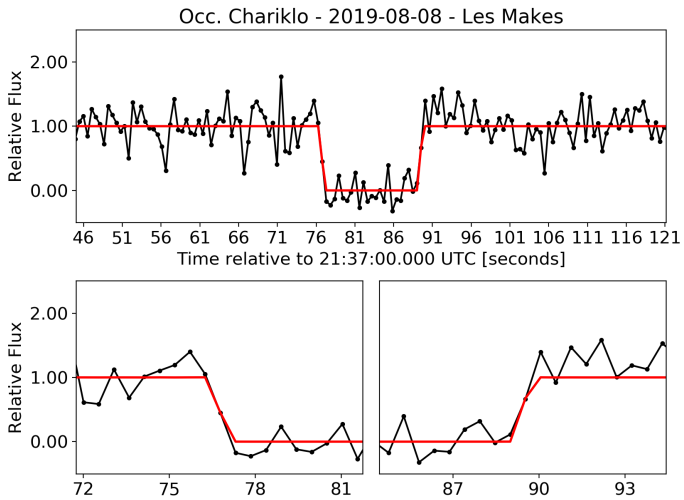

Fig. F.5. Light curve obtained at Les Makes on 2019 August 08.

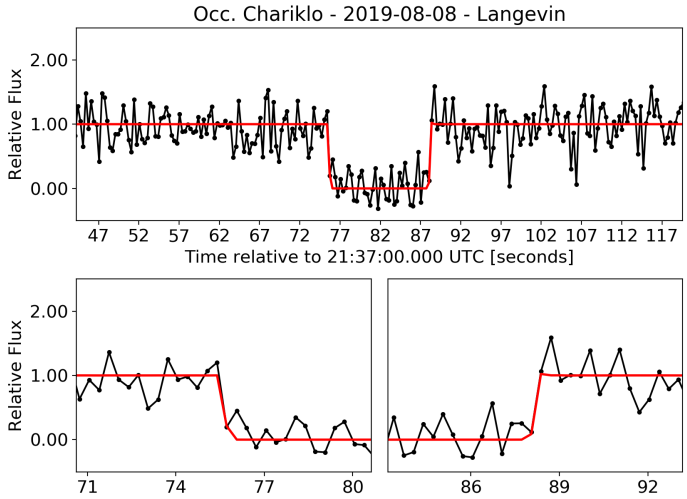

Fig. F.6. Light curve obtained at Langevin on 2019 August 08.

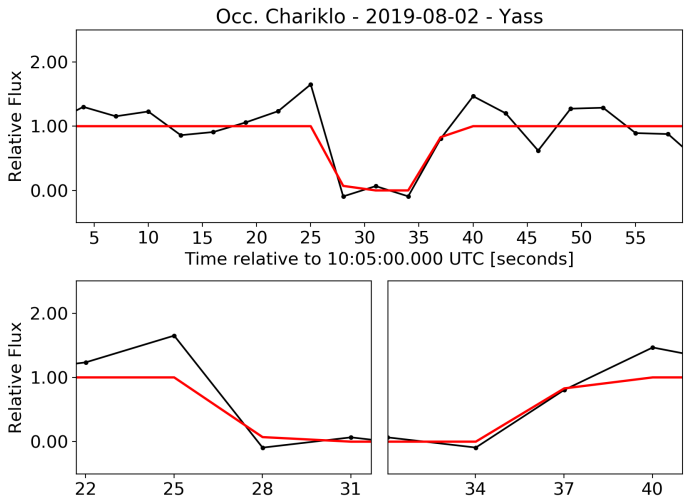

Fig. F.7. Light curve obtained at Yass on 2019 August 02.

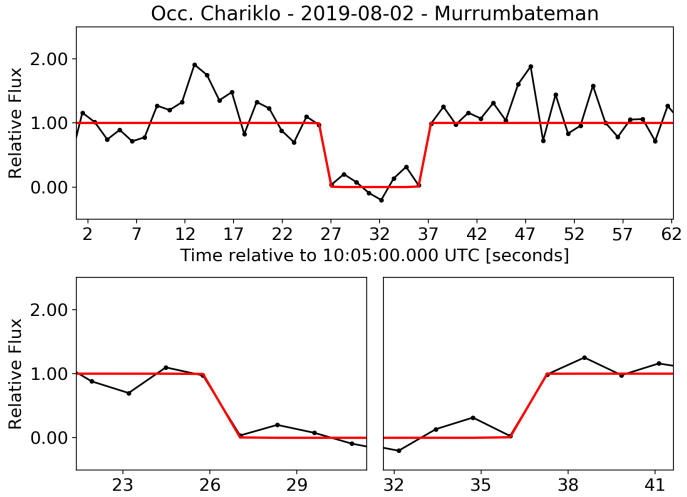

Fig. F.8. Light curve obtained at Murrumbateman on 2019 August 02.

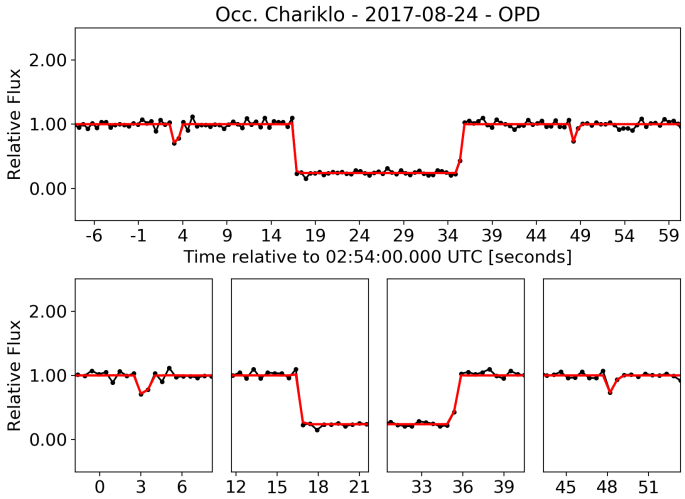

Fig. F.9. Light curve obtained at OPD on 2017 August 24.

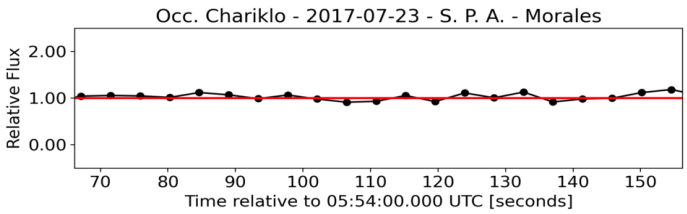

Fig. F.10. Light curve obtained at San Pedro de Atacama by Morales on 2017 July 23.

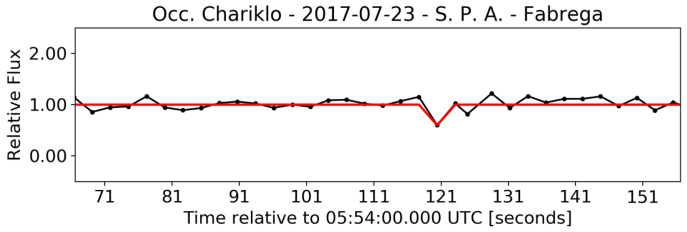

Fig. F.11. Light curve obtained at San Pedro de Atacama by Fabrega on 2017 July 23.

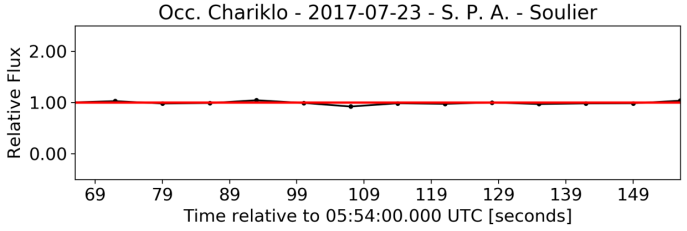

Fig. F.12. Light curve obtained at San Pedro de Atacama by Soulier on 2017 July 23.

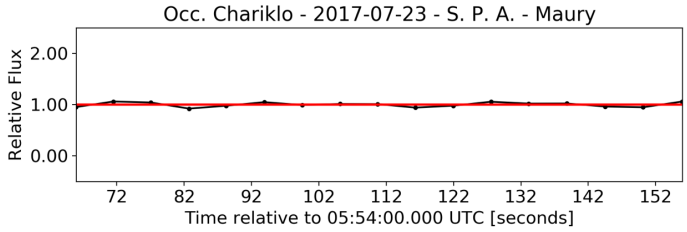

Fig. F.13. Light curve obtained at San Pedro de Atacama by Maury on 2017 July 23.

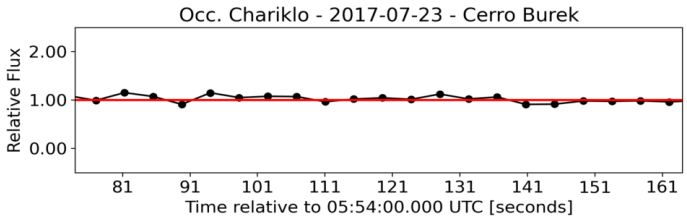

Fig. F.14. Light curve obtained at Cerro Burek on 2017 July 23.

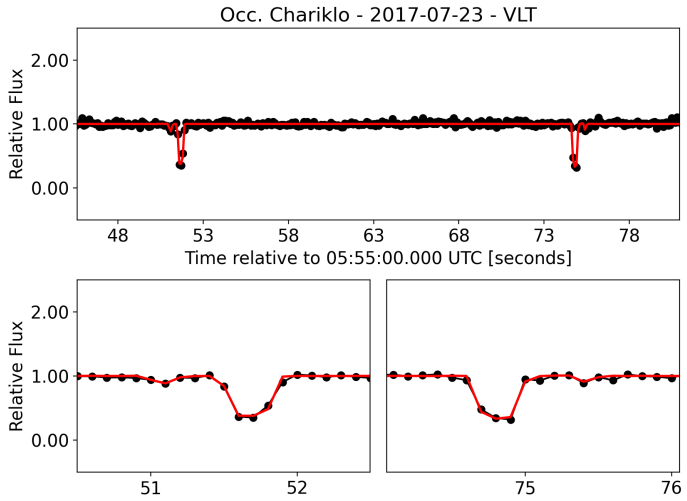

Fig. F.15. Light curve obtained at the VLT on 2017 July 23.

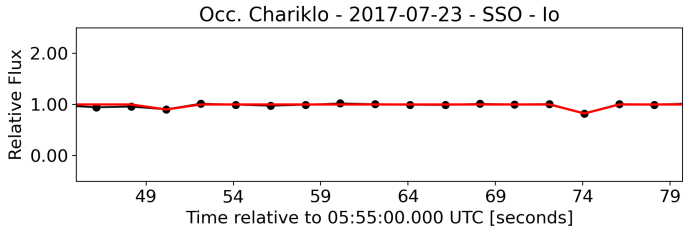

Fig. F.16. Light curve obtained at the SSO - Io on 2017 July 23.

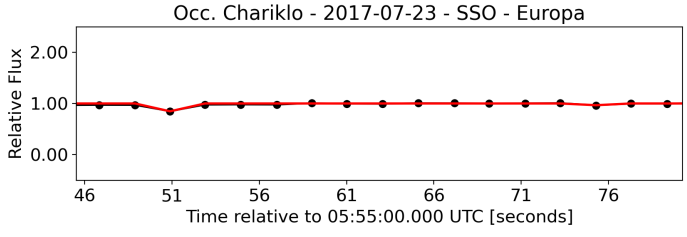

Fig. F.17. Light curve obtained at the SSO - Europa on 2017-07-23.

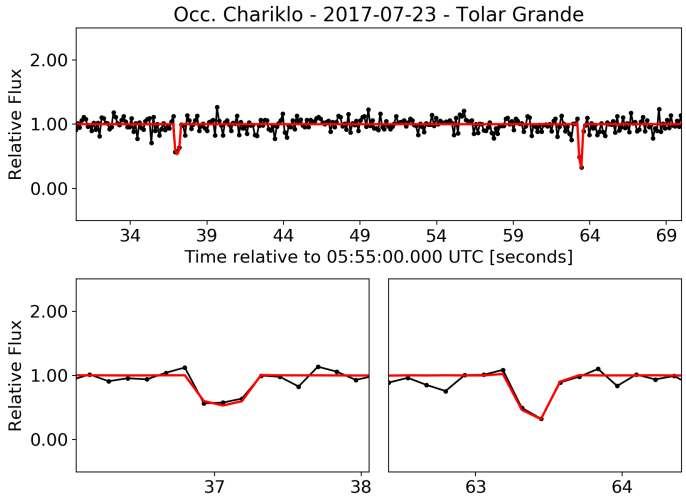

Fig. F.18. Light curve obtained at Tolar Grande on 2017 July 23.

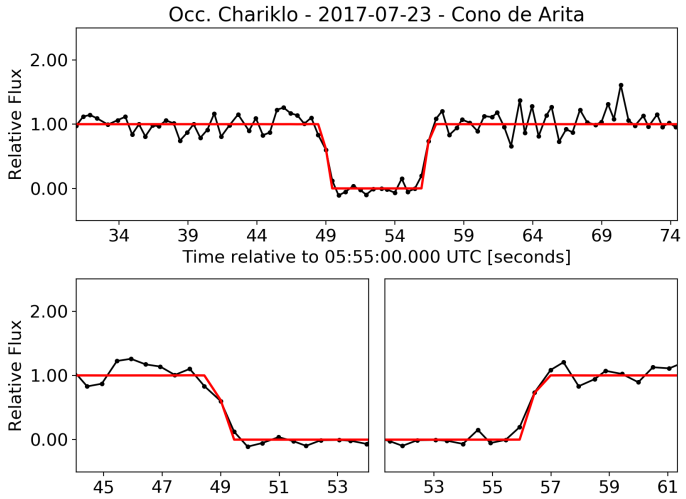

Fig. F.19. Light curve obtained at Cono de Arita on 2017 July 23.

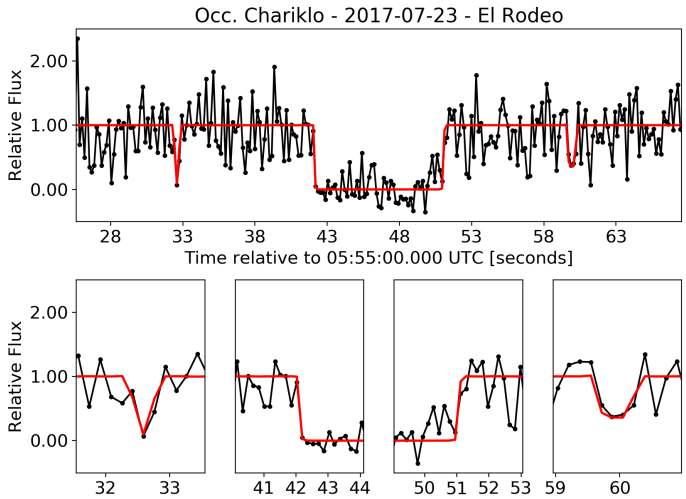

Fig. F.20. Light curve obtained at El Rodeo on 2017 July 23.

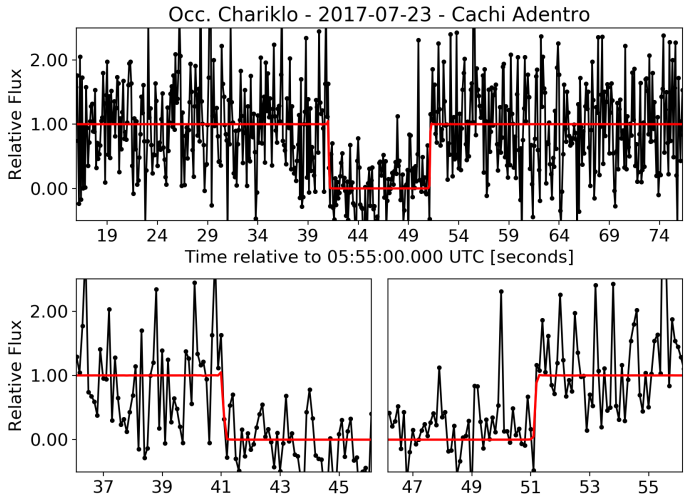

Fig. F.21. Light curve obtained at Cachi Adentro on 2017 July 23.

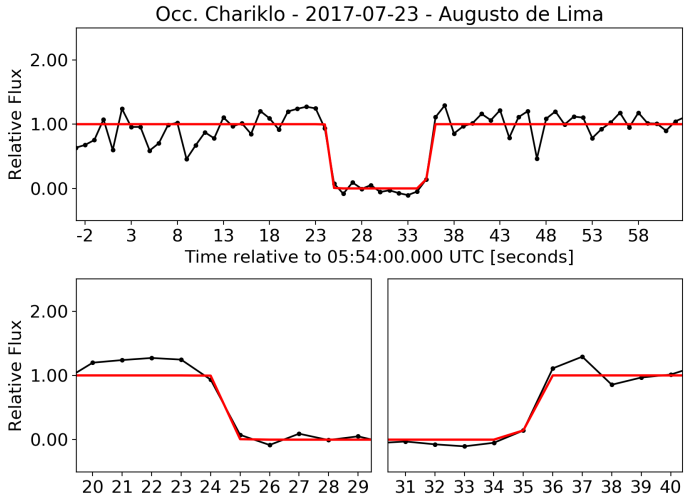

Fig. F.22. Light curve obtained at Augusto de Lima on 2017 July 23.

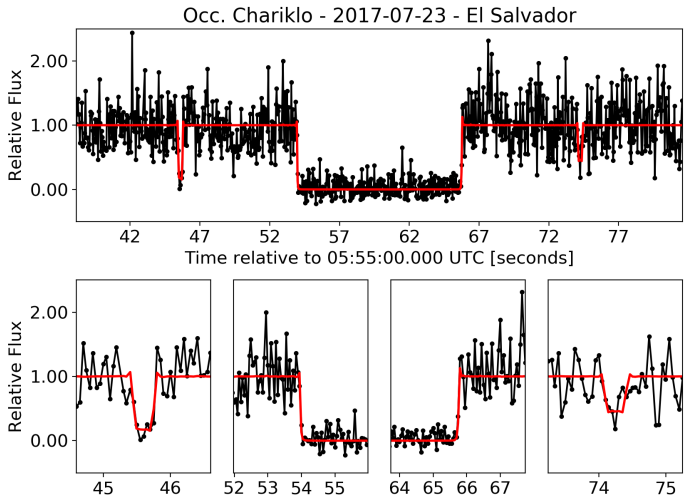

Fig. F.23. Light curve obtained at El Salvador on 2017 July 23.

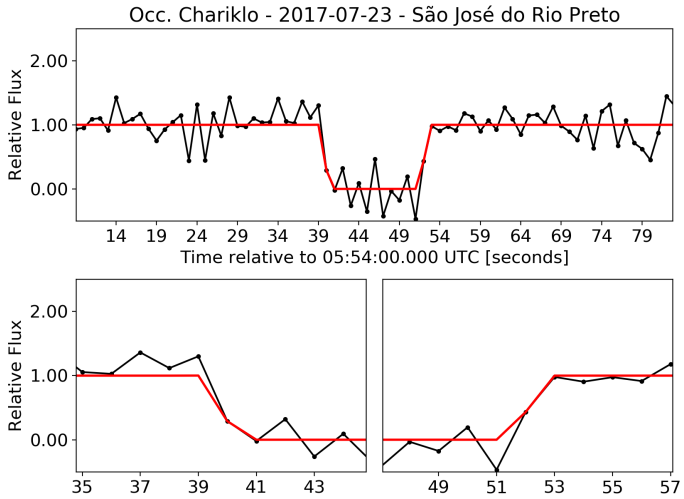

Fig. F.24. Light curve obtained at São José do Rio Preto on 2017 July 23.

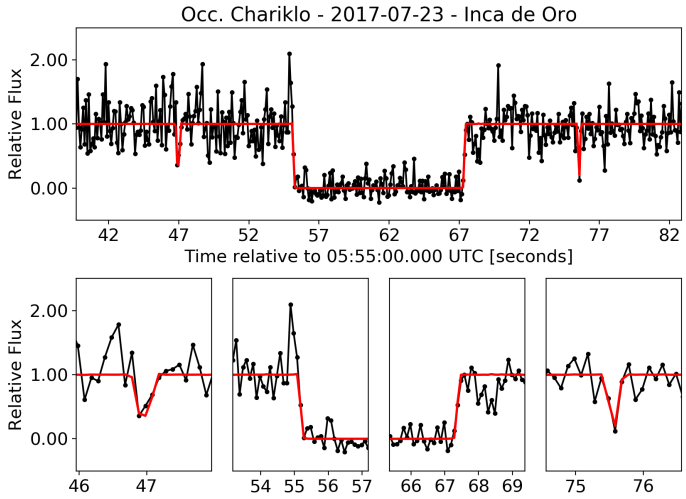

Fig. F.25. Light curve obtained at Inca de Oro on 2017 July 23.

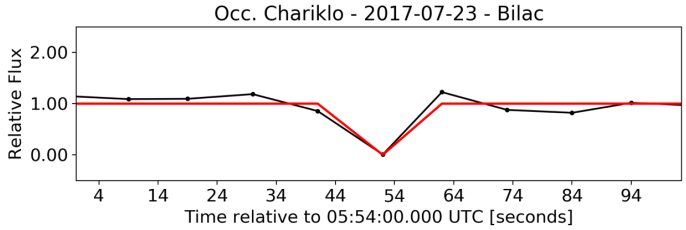

Fig. F.26. Light curve obtained at Bilac on 2017 July 23.

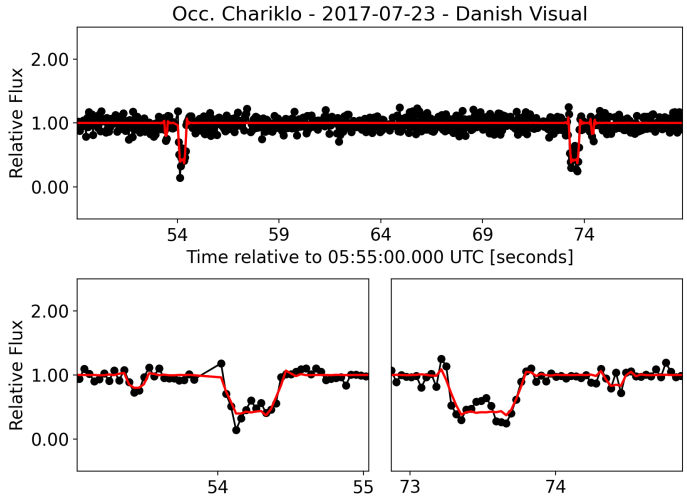

Fig. F.27. Light curve obtained with Danish with the Visual band on 2017 July 23.

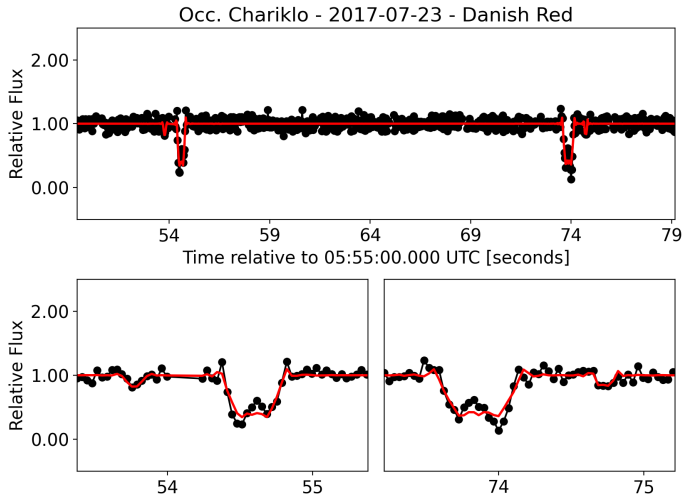

Fig. F.28. Light curve obtained with Danish with the Red band on 2017 July 23.

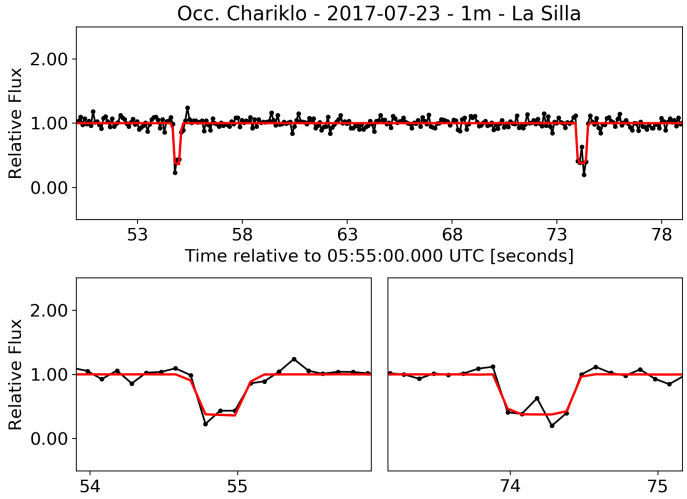

Fig. F.29. Light curve obtained with the 1m telescope in La Silla on 2017 July 23.

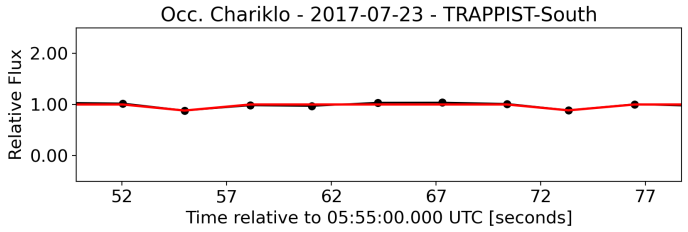

Fig. F.30. Light curve obtained with TRAPPIST-South on 2017 July 23.

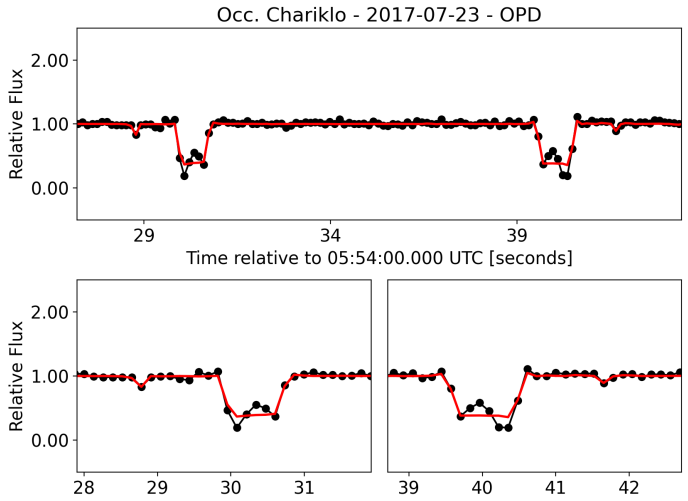

Fig. F.31. Light curve obtained at the OPD on 2017 July 23.

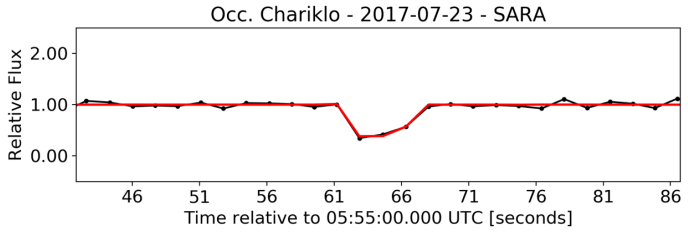

Fig. F.32. Light curve obtained with SARA on 2017 July 23.

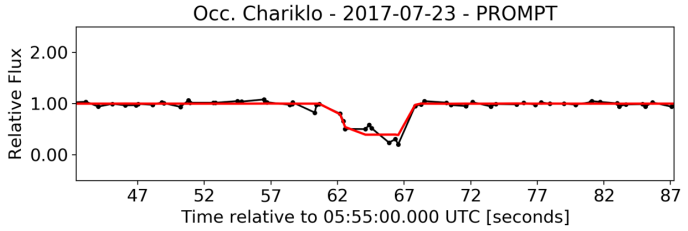

Fig. F.33. Light curve obtained with PROMPT on 2017 July 23.

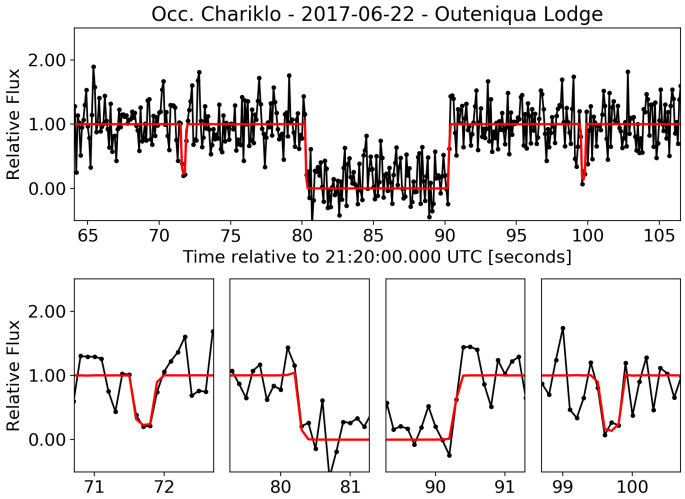

Fig. F.34. Light curve obtained at Outeniqua Lodge on 2017 June 22.

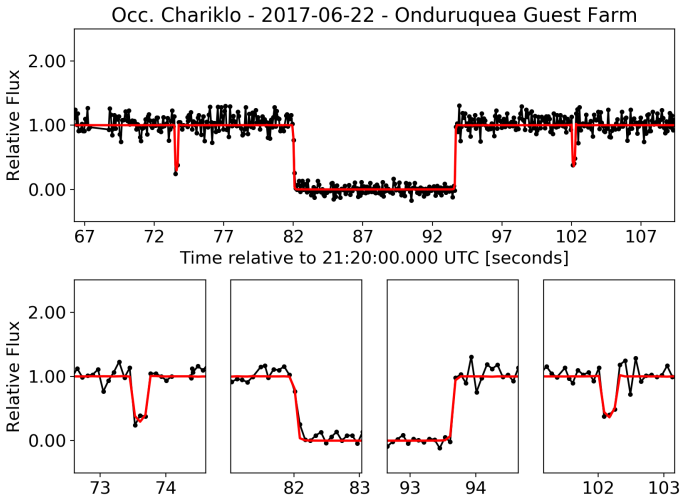

Fig. F.35. Light curve obtained at Onduruquea Guest Farm on 2017 June 22.

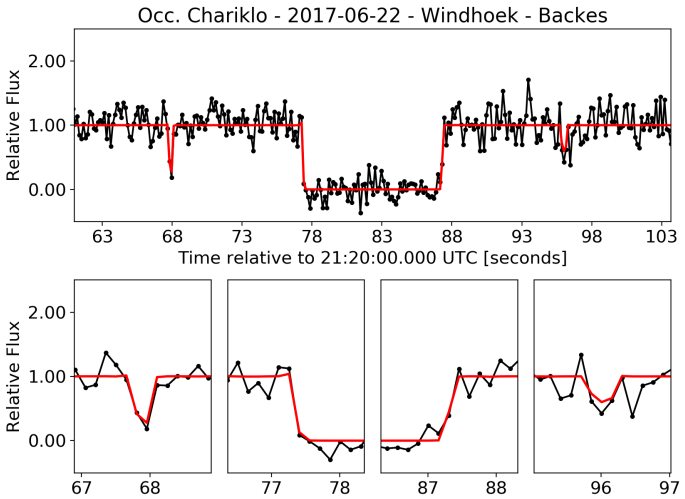

Fig. F.36. Light curve obtained at Windhoek by Backes on 2017 June 22.

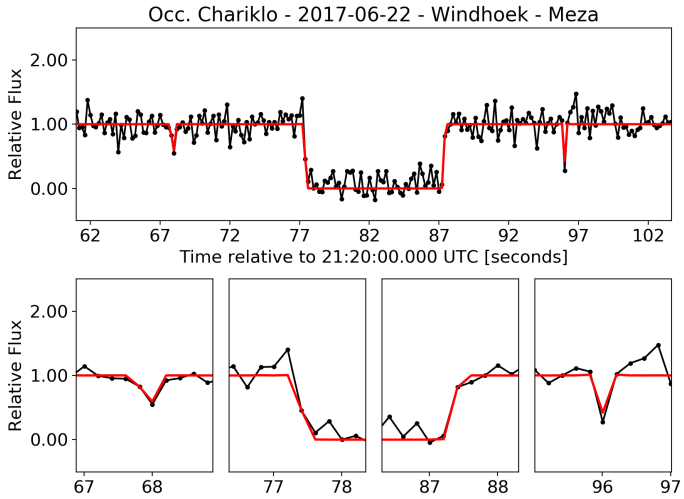

Fig. F.37. Light curve obtained at Windhoek by Meza on 2017 June 22.

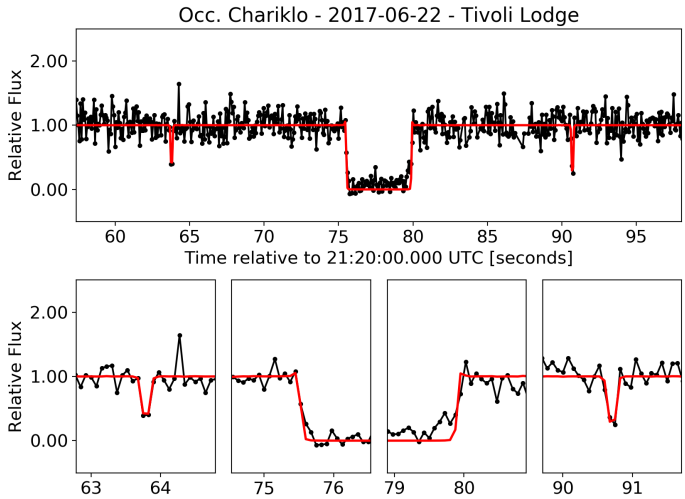

Fig. F.38. Light curve obtained at Tivoli Lodge on 2017 June 22.

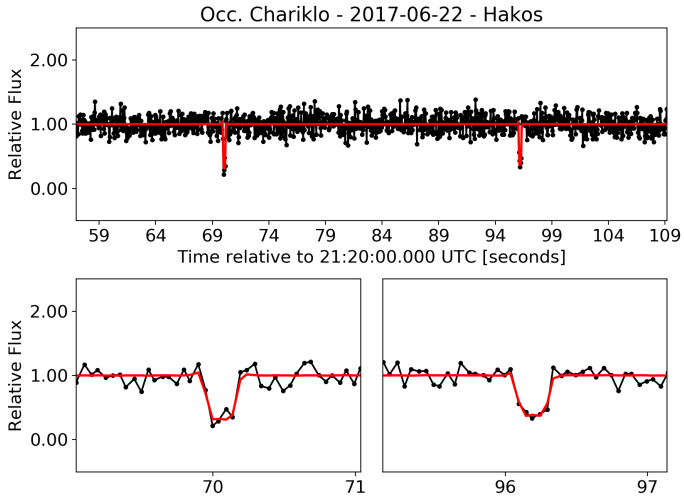

Fig. F.39. Light curve obtained at Hakos on 2017 June 22.

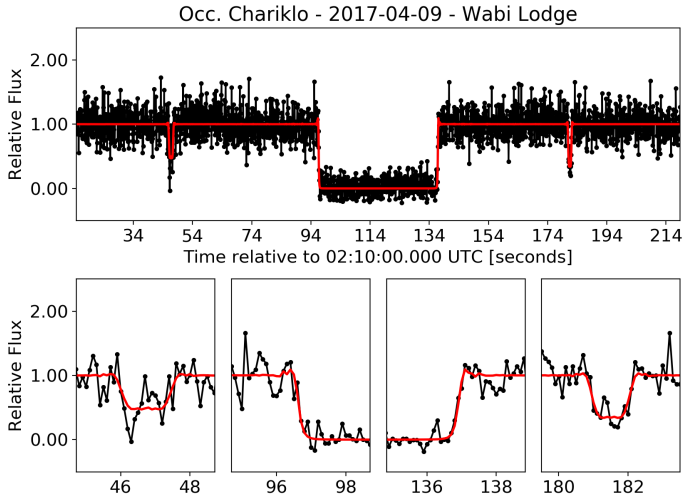

Fig. F.40. Light curve obtained at Wabi Lodge on 2017 April 09.

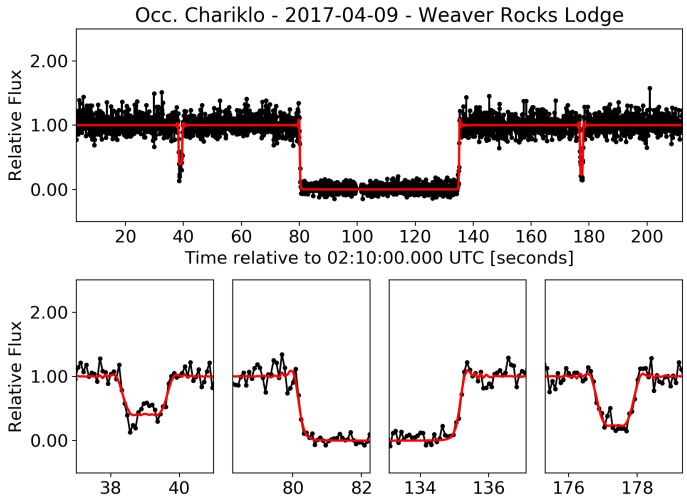

Fig. F.41. Light curve obtained at Weaver Rocks Lodge on 2017 April 09.

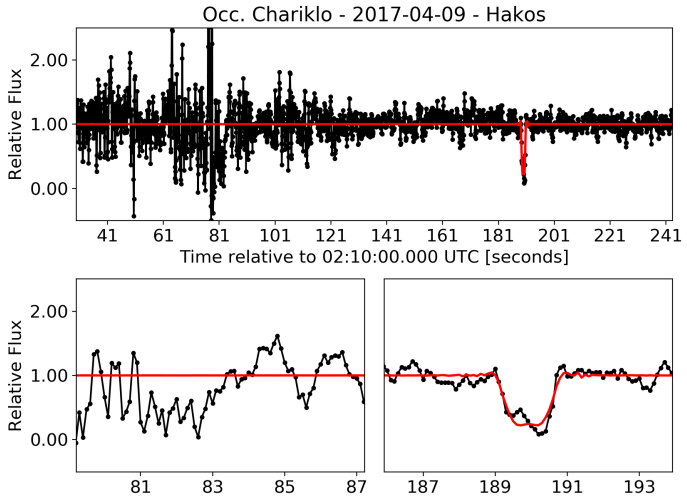

Fig. F.42. Light curve obtained at Hakos on 2017 April 09.